Vortex dynamics in classical Josephson junction arrays: models and recent experimental developments

1998 J. Phys.: Condens. Matter 10 1453

(http://iopscience.iop.org/0953-8984/10/7/002)

J. Phys.: Condens. Matter **10** (1998) 1453–1485. Printed in the UK PII: S0953-8984(98)79655-9

REVIEW ARTICLE

Vortex dynamics in classical Josephson junction arrays: models and recent experimental developments

José C Ciria† and C Giovannella‡

† Departamento de Fisica Teórica, Universidad de Zaragoza C/Pedro Cerbuna 12, 50010 Zaragoza, Spain

‡ Dipartimento di Fisica, Sezione INFN and Sezione INFM dell'Università di Roma Tor Vergata, Via della Ricerca Scientifica 1, 00133 Roma, Italy

Received 20 October 1997

Abstract. This review deals with the recent progress achieved in the understanding of vortex dynamics in discrete arrays of classical Josephson junctions, JJAs. We first give an up-to-date overview of the discrete models currently used to describe the physics of JJAs: the 'JJ array formalism', the discretized version of the sine–Gordon equation and the Frenkel–Kontorova model. Special emphasis is put on the recent reformulation of the screening term that makes use of the full-inductance matrix. The relationship between the phase and the vortex–particle dynamics is also discussed. An overview of the 'state of the art' in the understanding of the single-vortex dynamics in overdamped JJAs follows; the dependence of the motion of the vortex on its size (i.e. on the screening strength, the sample geometry and the coupling anisotropy, E_{Jx}/E_{Jy}) and, also, on the bias current is pointed out and discussed. A peculiar phenomenon, alternate-vortex motion, is also briefly illustrated. Subsequently, we review the single-vortex dynamics in underdamped JJAs. A short description of the conditions that lead to the observation of anomalous dissipation, vortex reflection, ballistic vortex motion, resonances, instabilities and row switching is given. To conclude, we discuss open problems and future perspectives of the research on JJAs.

1. Introduction

Arrays of Josephson junctions (JJAs), see figure 1, constitute one of the most intriguing examples of coupled non-linear oscillators [1, 2]. The diffuse interest in such complex systems is due not only to the richness of their physics (the macroscopic quantum phenomena, phase transitions, locking and chaos etc) which finds counterparts in many physical and biological systems [3], but also to the possibility of using JJAs in the production of useful cryoelectronic devices with unique properties and extremely low power consumption: Josephson voltage standards [4], fast logic elements [5], neural networks [6] and photofluxonic detectors [7, 8] (based on overdamped JJAs), oscillators and other hyperfrequency cryodevices (based, instead, on underdamped JJAs) [9] and vortex-flow transistors [10].

During the last five to ten years the number of publications devoted to the JJAs has continuously increased. The reasons for this are as follows.

(a) *An improved reliability of the lithographic and fabrication processes* which allows a much higher degree of integration than before.

Nowadays, cryoelectronics circuits may contain up to some hundreds of Josephson junctions, whose physical parameters are identical within an acceptable dispersion; the

0953-8984/98/071453+33$19.50

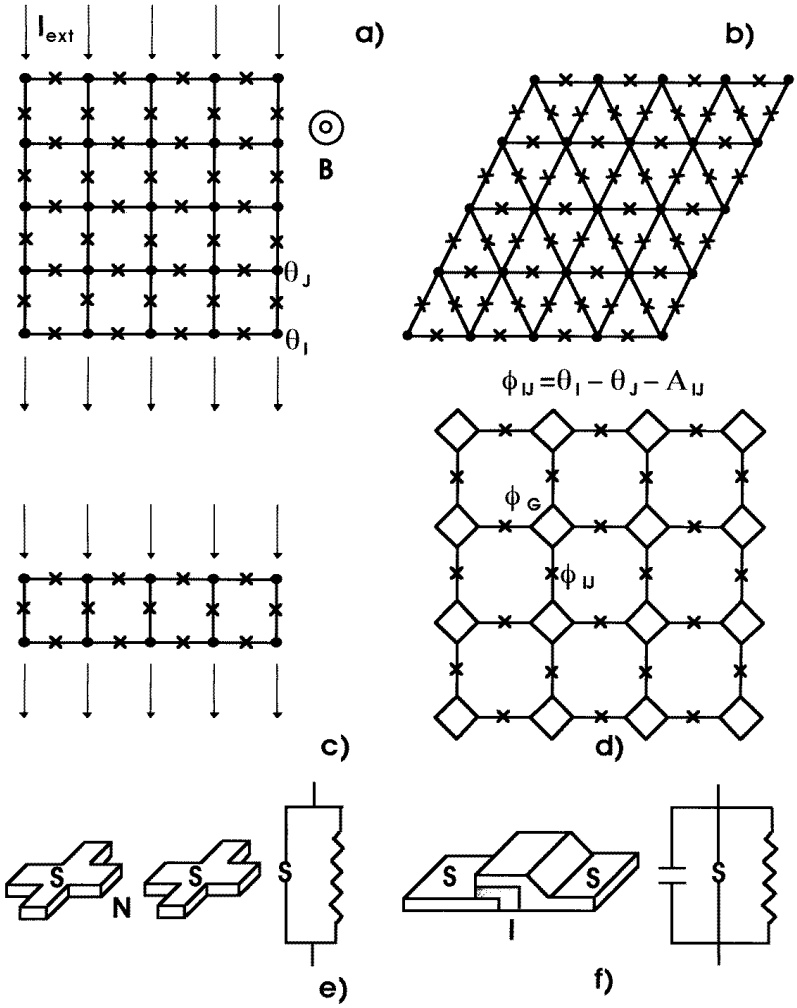

Figure 1. Examples of JJ arrays: (a) a 2D square network; (b) a 2D triangular network; (c) a JJ ladder (one JJ is placed on each branch of the array and each grain is characterized by a single phase, θ_j); (d) 2D granular superconductors: the grains are now extended and the phase changes along the grain. The ϕs are the gauge-invariant phase variations along the junction (J) and along the grain (G): $\phi_J = \theta_i - \theta_j - A_{ij}$. A_{ij} is the contribution due to the vector potential and it is defined in the text. (e) and (f) are schematic representations of, respectively, a SNS and a SIS Josephson junction with their equivalent electric circuits (see the text for more details). The external magnetic field, B, applied perpendicularly to the samples generates a frustration $f = BS/\Phi_0$ where S is the surface of the plaquette.

spread of such parameters is usually kept within a few per cent of their average values. Reliable fabrication processes make it possible to compare, with a certain degree of confidence, experimental results obtained for real systems and computer simulations of model systems.

(b) *The recent availability of inexpensive personal workstations.*

Simulations of large discrete systems, like the JJAs, based on realistic models, have been quite impossible for a long time (they were too expensive and time consuming);

now, on the other hand, a few thousands of dollars are sufficient to buy a computer powerful enough to allow the simulation of both the static and the dynamical properties of JJAs with geometrical dimensions comparable to those of the real systems employed in experiments. Numerical simulations are essential if one wishes to study the dynamics of systems composed of many coupled non-linear oscillators, like the JJAs, for which there do not exist analytical descriptions and for which the interpretation of the experimental data is not at all straightforward.

(c) *The discovery of high-T_c superconductors* which renewed the interest in superconducting cryoelectronics—with the hope of producing devices able to operate at liquid nitrogen temperatures.

The fabrication of reliable high-T_c superconducting junctions is still made difficult by their intrinsic short coherence length which imposes the requirement of controlling the junction parameters on a scale much shorter than is currently possible with up-to-date fabrication technologies; JJAs, consequently, have been employed to model and study the effect of the 'disorder' in the high-T_c superconducting devices [11]. In addition, most of the high-T_c superconductors are materials in which the bidimensional superconducting layers seem to be coupled along the z-axis through the Josephson effect. High-T_c materials, thus, can be likened to stacks of extended Josephson junctions [12] and can be modelled, again, by means of JJAs, although only anisotropic ones.

All of the interesting applications of JJAs in cryoelectronics rely on the formation and on the displacement of special quasi-solitonic excitations of the gauge-invariant phase: the so-called vortices/antivortices. A vortex obeys the fluxoid quantization rule: the sum of the gauge-invariant phase circulation along any path enclosing the vortex plus the magnetic flux through the surface defined by this path has to be always $2n\pi$ where n is an integer; see figure 2.

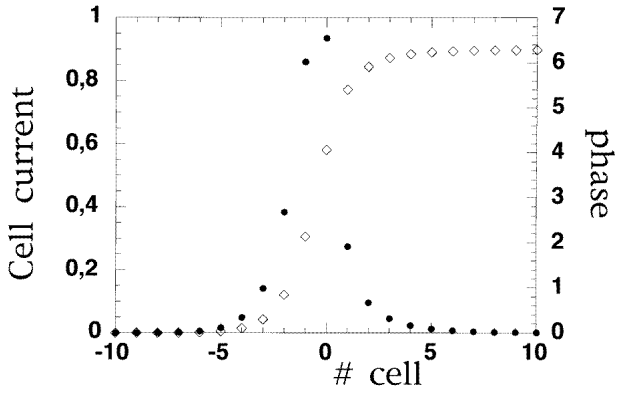

Figure 2. An example of topological excitations of the JJA phase configuration of a ladder, 32×2: the 2π phase variation ($\diamond$) and the associated voltage peak ($\bullet$). The topological excitations are travelling from left to right.

Vortex–antivortex couples develop whenever a perturbation breaks the symmetry of the flowing current on a local scale and acts for long enough to transfer into the system the needed formation energy. As an example, in biased samples, vortices form because of current spikes, geometrical defects, an inhomogeneous spatial distribution of the bias current, a perturbation caused by an incoming photon and so on [8].

Why are vortices/antivortices so relevant for cryoelectronic devices?

In overdamped JJAs, as we will show later, vortices can be likened to massless particles; their displacement can be used to transfer elemental bits of information. Indeed, by controlling the vortex formation, transmission, trapping and annihilation one can build very fast digital circuits (having clocks operating at some hundreds of GHz) and, it is hoped, very fast computer facilities [5].

In underdamped JJ systems, on the other hand, the vortices acquire a mass (i.e. a kinetic contribution to their energy) and can be reflected at the border of the sample. One can use the periodic reflections of the vortices to fabricate oscillators able to emit and detect electromagnetic radiation in the hyperfrequency domain. Unfortunately, the electromagnetic power emitted by a single oscillator (vortex/antivortex) is quite low (of the order of a microwatt) as, also, is its output impedance (a few ohms) [9].

In JJAs, however, under certain experimental conditions, several vortices may couple with each other giving rise to a coherent motion (a dynamical locked state) that, in principle, should lead to an electromagnetic emission whose power is proportional to N^2, where N is the number of oscillators involved in the process. In addition, due to the array geometry, the output impedance of the devices is also expected to increase up to values reasonable enough to allow their integration in hybrid circuits.

At this point we have, we hope, convinced the reader that a careful investigation of vortex dynamics is essential if one is to achieve a correct understanding of the JJA physics and, as a consequence, to describe in a correct manner the operational mode of the cryo-devices based on JJAs.

In the past, single-vortex dynamics has been the subject of a number of reviews; all of them, however, dealt with systems that represent the continuous counterpart of the JJAs: the long and the stacked Josephson junctions [13–16]. The same level of attention has not been given to the description of the vortex dynamics developed within the framework of 'JJ array formalism'. As far as we are aware, there are many interesting articles available describing research on the subject, but no reviews. In view of this, perhaps it is the right time to make an effort to give a review of this area.

Further motivation for writing this article was provided by the need to review the important progress recently made in the understanding of the JJA physics related to the reformulation of the 'JJ array formalism' to include a full-screening term—a reformulation that was first implemented by Phillips *et al* [17] and then, in an independent way, by other groups [18, 19].

Now, as a result of the introduction of the full-inductance matrix, the mutual inductance of the currents flowing in the array (the Biot–Savart law) can be worked out in a precise manner and it is no longer introduced as an *ad hoc* mean-field quantity [20]. As regards the XY-model, one has to consider the development of the 'JJ array formalism' to include the full-inductance matrix as a decisive step towards a more realistic description of the JJA physics: it allowed for the introduction of a tunable and finite penetration depth ($\lambda_\perp$).

The review is organized as follows.

The first part of the next section introduces the reader to the 'JJ array formalism' as currently used, while the second part of the section will be dedicated to comparing the 'JJ array formalism' with other discrete models such as the sine–Gordon and Frenkel–Kontorova ones and to discussing the equivalence between the phase and the vortex formulation of the JJA dynamics.

Sections 3 and 4 then deal with single-vortex dynamics, respectively in overdamped and underdamped JJAs. Experiments and numerical simulations are compared and discussed.

Finally, in the last section, we briefly point out open problems and future lines of development.

2. The discrete 'JJ array formalism'

2.1. The discrete JJA Lagrangian

The Lagrangian of a Josephson junction array subjected to the action of an external forcing term (a bias current applied along the y-direction) and to a local random force (the thermal noise) is given by

$$L = E_J \left\{ \sum_{ij} (\cos\phi_{ij} - 1) + \frac{\beta_c}{2} \sum_{ij} \dot{\phi}_{ij}^2 + \sum_{i;kl} i_{ext;i} [(DG)^{-1} D]_{i;kl} \phi_{kl} - \sum_{ij} \tilde{i}_{ij} \phi_{ij} \right.$$
$$- \frac{1}{2} \sum_{p,q} (R\phi + 2\pi f)_p \Lambda^{-1}_{p,q} (R\phi + 2\pi f)_q$$
$$\left. - \sum_{p,i} (R\phi + 2\pi f)_p (\Lambda^{-1}\Delta - (RR^{\mathrm{T}})^{-1} RM)_{p,i} i_{ext;i} \right\}. \tag{1}$$

Here, $\phi_{ij} = \theta_i - \theta_j - a_{ij}$ is the gauge-invariant phase difference along the junction ij. θ_i is the phase of the pseudo-wavefunction describing the state of grain i, $|\Psi_i| \exp(\mathrm{i}\theta_i)$, where $|\Psi_i|^2 = n_s$ (n_s is the density of the superconducting pairs and $|\Psi_i|$ is constant for all of the grains: $|\Psi_i| = |\Psi|$). a_{ij} is related to the vector potential $\boldsymbol{A}$ through

$$a_{ij} = \frac{2\pi}{\Phi_0} \int_i^j \boldsymbol{A} \cdot \mathrm{d}\boldsymbol{x}.$$

i, j stand for nearest-neighbour points and p runs over the plaquettes of the array. Λ and Δ will be defined further on in this section.

The physical meaning of operators P_r, D and G is simple to understand. As is well known, any vector field can be expressed as the sum of a solenoidal field plus an irrotational one (with vanishing divergence and curl, respectively). We call the operator that, applied to any field, selects its solenoidal (irrotational) component P_r (P_d). These operators can be expressed as $P_d = G(DG)^{-1}D$ (where G and D are discrete versions of the operator gradient and divergence) and $P_r = R^{\mathrm{T}}(RR^{\mathrm{T}})^{-1}R$ (with R the discrete rotational operator). Of course, $RG = 0$, $P_r P_d = 0$, $P_r P_r = P_r$, $P_d P_d = P_d$, $P_r + P_d = 1$. We have chosen the London gauge ($\boldsymbol{\nabla} \cdot \boldsymbol{A} = 0$), so $(DG)^{-1} D\phi = \theta$, $(P_d\phi)_{ij} = \theta_i - \theta_j$ and $(P_r\phi)_{ij} = -a_{ij}$.

The ϕ_{ij} are connected to the normalized junction voltage drop $v = (2e/h)V$ measurable at the junction through the Josephson relation: $\dot{\phi}_{ij} = 2\pi v$.

$E_J = \Phi_0 I_c / 2\pi$ is the junction coupling energy and Φ_0 is the elemental quantum of flux. ($\Phi_0 = h/2e = 2.068 \times 10^{-15}$ V s.) $\Lambda_{ij;kl}$ is the full-inductance matrix, normalized to $\Phi_0/(2\pi I_c)$. $\beta_c = 2eI_cR^2C/\hbar$ is the McCumber parameter where R and C are respectively a characteristic shunt resistance and a capacitance (see further on for their definition). $\tilde{i}$ is a thermally induced noise current. The currents are normalized to the critical current of the junction, I_c.

$$\tau = \frac{2eR_eI_c}{\hbar} t$$

is the normalized time.

Equation (1) has been written using the conjugate pair of variables ϕ and $\dot{\phi}$ to stress that the gauge-invariant phases are the relevant dynamical variables (the equivalence between the phase and the vortex dynamics is discussed further on).

Let us now examine one by one the terms of the Lagrangian. The first one accounts for the energy stored in the Josephson junctions. The second term represents the energy stored in the electric field; it depends both on the capacitance of each single island with respect to

the ground, C_i, and on the capacitance between the nearest-neighbour islands, C_{ij}, i.e. the capacitance of the junctions. Since C_{ij} is always much larger than C_i [22], in the rest of this review the contribution due to the self-capacitance will be neglected.

The third and fourth terms are related to the work done on the system by the external current generator (either dc or ac) and by a white-noise current (that takes into account the thermal noise generated by the resistors). Usually this latter is chosen such that

$$\langle i_{ij}(\tau)\rangle = 0$$

and

$$\langle i_{ij}(\tau+\tau_0)i_{kl}(\tau)\rangle = \frac{2k_BT}{R_{ij}}\delta(\tau_0)\delta_{ij;kl}.$$

The last terms of equation (1) represent, as stated in the introduction, the main difference between the XY-formalism, where $\lambda_\perp$ is always taken equal to ∞ [21], and the 'JJ array formalism', where $\lambda_\perp$ can assume finite values. It is related to the energy stored in the magnetic field due to the mutual inductance of branches of the array. The normalized inductance matrix (Λ) connects the induced magnetic flux through the plaquettes to the mesh currents defined on each cell (for a definition of mesh current, see figure 1):

$$\Phi_{ind;p} = \sum_{p,q}\Lambda_{p,q}i_q. \tag{2}$$

The vector potential includes the contributions from both the external and the internal magnetic fields:

$$a_{ij} = \frac{2\pi}{\Phi_0}\int_i^j (\boldsymbol{A}_{ij;ext} + \boldsymbol{A}_{ij;int})\cdot \mathrm{d}\boldsymbol{r}. \tag{3}$$

The flux of the external magnetic field through plaquette p is

$$(Ra_{ext})_p = 2\pi f_p = \frac{2\pi}{\Phi_0}\int_p \boldsymbol{B}_{ext}\cdot \mathrm{d}\boldsymbol{S} \tag{4}$$

where $\boldsymbol{S}$ is normal to the surface of the plaquette, S, and $\boldsymbol{B}_{ext} = \boldsymbol{\nabla}\times\boldsymbol{A}_{ext}$.

The $a_{ij;int}$ are due to the currents circulating in the array (i_{ij}) [19]:

$$a_{ij;int} = \sum_{kl}\frac{1}{4\pi\lambda_\perp}\mathrm{ff}_{ij;kl}i_{kl} \tag{5}$$

where $\lambda_\perp$ is the normalized effective penetration depth of the array [17]:

$$\lambda_\perp = \frac{1}{2\pi}\frac{\Phi_0}{\mu_0 I_c l_a} \tag{6}$$

with l_a the lattice spacing of the array. $\mathrm{ff}_{ij;kl}$ is a form factor matrix related to the geometry of the array. In most cases all of the non-diagonal elements of the ff matrix can be assumed to depend only on the relative distance between the links of the array, $r = r_{ij} - r_{kl}$, and not on the shape of the Josephson junction. The self-term, on the other hand, diverges when $r \to 0$ and this forces us to consider the particular geometry of the junction in order to introduce the appropriate geometrical cut-off [19].

The link currents are related to the mesh currents through $\boldsymbol{i}_{link} = R^{\mathrm{T}}\boldsymbol{i}_{mesh} + M\boldsymbol{i}_{ext}$. $M_{ij;k} = 1$ if k is a site belonging to the first row, and ij is a vertical link aligned with it; otherwise, $M_{ij;k} = 0$. The Biot–Savart equation (5) can be expressed as

$$\Phi_{ind} = \Lambda\boldsymbol{i}_{mesh} + \Delta\boldsymbol{i}_{ext} \Rightarrow \boldsymbol{i}_{mesh} = \Lambda^{-1}(\Phi_{ind} - \Delta\boldsymbol{i}_{ext}) \tag{7}$$

where the matrix Δ is defined as

$$\Delta = \frac{1}{4\pi\lambda_\perp} R\mathrm{ff}M \tag{8}$$

and Λ can be easily related to ff:

$$\Lambda = \frac{1}{4\pi\lambda_\perp} R\mathrm{ff}R^{\mathrm{T}}. \tag{9}$$

We stress again that by means of equation (5) the current contribution to the local vector potential, $a_{ij;int}$, can be worked out exactly for each link and is no longer introduced as a mean-field quantity. This difference may be quite important, especially for finite 2D systems with relatively small dimensions, such as the ones commonly used in experiments.

Since in this review we deal with arrays for which charging effects and the fluctuations of the amplitude of the superconducting order parameter are negligible, we have dropped Lagrangian terms like $-\hbar n_s P_d \dot{\theta}_i$ and $-(n_s - \tilde{n}) q P_d V_i$ that are related to the displacement of charges (n_s is the density of the superfluid, $\tilde{n}$ is the background charge density and V_i is the scalar potential); by applying Lagrangian equations to these terms, the Josephson voltage relationship can be obtained [23].

2.2. The equation of motion

The Euler–Lagrange equations for our system are

$$\frac{\mathrm{d}}{\mathrm{d}t}\left(\frac{\partial L}{\partial \dot{\phi}_{ij}}\right) - \frac{\partial L}{\partial \phi_{ij}} + \frac{\partial \mathcal{F}}{\partial \dot{\phi}_{ij}} = 0 \tag{10}$$

where $\mathcal{F}$ is Rayleigh's function giving the ohmic dissipation

$$\mathcal{F} = \frac{1}{2}\sum_{ij;kl} \dot{\phi}_{ij}(s)\alpha_{ij;kl}\dot{\phi}_{kl}(s). \tag{11}$$

α is an operator defined as

$$\alpha = G(DG)^{-1} r^{-1} (DG)^{-1} D + R^{-1} \tag{12}$$

where r and R are diagonal operators whose elements are, respectively, R_i (the resistance of the superconducting island i with respect to the ground) and R_{ij} (the resistance between the ith and the jth islands, i.e. the junction resistance due to the tunnelling of the quasi-particles for SIS junctions and the normal-state resistance for the SNS junctions). In general one neglects the self-resistance (the resistive shunted model, RSJ) and, also, the coupling between the tunnelling quasi-particles and the environment; one should note, however, that the island resistance with respect to the ground is the basic dissipative term in the TDGL model [25], while the coupling to the environment may lead to a redefinition of E_J for junctions with a normal resistance of the order of 100 Ω (the environment impedance) [24]. Moreover, almost always one assumes a constant R_{ij}, neglecting the dependence of R_{ij} on ϕ; basically, this is equivalent to shunting the junction with an external resistance R_e smaller than the junction resistance. To take account of the dependence of $R_{ij}(\phi) = 1/G(\phi)$ on ϕ one can use the following expression [26]:

$$G(V) = G_{sg} + (1 - G_{sg})[1 - \tanh K(1 - V/V_g)]/2$$

where G_{sg} is the ratio of the sub-gap conductance to the normal-state conductance, K is a constant and $v_g = 4I_c R_n/\pi$ is the gap voltage.

Another common approximation is that of neglecting the spatial distributions of the R_{ij} that may result from the limits of the fabrication process.

Thus, neglecting R_i and taking R_{ij} as a constant, from equation (10) one obtains a set of equations whose matrix form, in normalized units, is

$$\beta_c\ddot{\boldsymbol{\phi}} + \dot{\boldsymbol{\phi}} + \boldsymbol{i}_c \sin\boldsymbol{\phi} + \tilde{\boldsymbol{i}} - [G(DG)^{-1}]\boldsymbol{i}_{ext} - P_r M \boldsymbol{i}_{ext} + R^{\mathrm{T}}\Lambda^{-1}(R\boldsymbol{\phi} + 2\pi\boldsymbol{f}) + R^{\mathrm{T}}\Lambda^{-1}\Delta\boldsymbol{i}_{ext} = 0. \tag{13}$$

By considering the irrotational and solenoidal components of equation (13) one obtains the two sets of Kirchhoff and the Biot–Savart equations. In fact, by taking the divergence of equation (13) one has

$$D(\beta_c\ddot{\boldsymbol{\phi}} + \dot{\boldsymbol{\phi}} + \boldsymbol{i}_{c;\phi}\sin\boldsymbol{\phi} + \tilde{\boldsymbol{i}}) \equiv D\boldsymbol{i}_{link} = \boldsymbol{i}_{ext} \tag{14}$$

where the $\boldsymbol{i}_{link}$ are the currents flowing along the links. This vector equation reads, for each node i,

$$\sum_j \beta_c \frac{\mathrm{d}^2\phi_{ij}}{\mathrm{d}\tau^2} + \sum_j \frac{\mathrm{d}\phi_{ij}}{\mathrm{d}\tau} + \sum_j i_{c;ij}\sin(\phi_{ij}) + \sum_j \tilde{i}_{ij} - i_{i;ext} = 0. \tag{15}$$

On the other hand, by realizing that $G(DG)^{-1}\boldsymbol{i}_{ext} = G(DG)^{-1}D\boldsymbol{i}_{link} \equiv P_d\boldsymbol{i}_{link}$, and using $\boldsymbol{i}_{link} = R^{\mathrm{T}}\boldsymbol{i}_{mesh} + M\boldsymbol{i}_{ext}$, $P_r + P_d = 1$ and $P_d R^{\mathrm{T}} = 0$, we can group the first six terms in equation (13) to give

$$\boldsymbol{i}_{link} - G(DG)^{-1}\boldsymbol{i}_{ext} - P_r M\boldsymbol{i}_{ext} = R^{\mathrm{T}}\boldsymbol{i}_{mesh}. \tag{16}$$

Applying $(RR^{\mathrm{T}})^{-1}R$ to (13), one obtains the Biot–Savart equation (7).

It is worthwhile stressing that, since the nodes of the array are represented by point grains, fluxoid quantization is automatically fulfilled:

$$\sum_{ij\in p}\phi_{ij} + 2\pi f + \Phi_{ind} = 2n_p\pi. \tag{17}$$

$\sum_{ij\in\alpha}$ stands for the anticlockwise sum along the links of the α-plaquette and the ϕ_{ij} are restricted to varying in the interval $(-\pi, \pi]$. $\Phi = 2\pi f + \Phi_{ind}$ is the total flux through the cell.

It should be noted that in a recent paper Lucheroni [27] has shown that the dynamics of the mesh currents and that of the phases of the superconducting nodes can be separated by making the following substitution for the gauge-invariant phase: $\phi = D^{\mathrm{T}}\theta + (R_L)^{\mathrm{T}}i_{mesh}$ (a fact that implies the existence of two types of dynamics having different timescales, as clearly pointed out in reference [18]); if just the self-inductance of the cells is considered, then R_L can be factorized as LR, where L is the self-inductance. As a consequence a reduction in the number of coupled differential equations is obtained.

2.3. The JJA formalism and the granular superconductors

The 'JJ array formalism' and its Lagrangian allow us also to describe the case of weakly coupled granular superconductors for which the phases are not uniform inside each grain. To do this one should consider the intragranular currents and phase shifts. A way of implementing this is to describe each superconducting site as a plaquette; a supercurrent, linear in the phase, flows within it. Thus, we must generalize the gauge-invariant phases, currents and fluxes, to add new variables corresponding to the superconducting-grain links and cells:

$$\boldsymbol{\phi} \to \hat{\boldsymbol{\phi}} \equiv \{\boldsymbol{\phi}_J, \boldsymbol{\phi}_S\}$$
$$\boldsymbol{\Phi} \to \hat{\boldsymbol{\Phi}} \equiv \{\boldsymbol{\Phi}_J, \boldsymbol{\Phi}_S\}$$
$$\boldsymbol{i}_{link} \to \hat{\boldsymbol{i}}_{link} \equiv \{\boldsymbol{i}_{link;J}, \boldsymbol{i}_{link;S}\}$$
$$\boldsymbol{i}_{mesh} \to \hat{\boldsymbol{i}}_{mesh} \equiv \{\boldsymbol{i}_{mesh;J}, \boldsymbol{i}_{mesh;S}\}.$$

The intragranular currents are proportional to the gradient of the phase along the border of the grain: $i_{ij;S} = i\phi_{ij;S}$ where $i = n_s e\bar{h}/m$ (n_s is the density of superconducting pairs). The discrete operators used up to now must also be generalized. Now, the curl along a plaquette contains contributions both from Josephson and superconducting branches; see figure 1:

$$\begin{pmatrix} \Phi_J \\ \Phi_S \end{pmatrix} = -\hat{R}\begin{pmatrix} \phi_J \\ \phi_S \end{pmatrix} \qquad \hat{R} \equiv \begin{pmatrix} R & R_{JS} \\ 0 & R_{SS} \end{pmatrix}. \tag{18}$$

Inside the grain, the magnetic flux is 0 ($R_{SS}\phi_S = 0$), and thus ϕ_S is an irrotational field ($\phi_S = G_{SS}V$). On the other hand, $\hat{\boldsymbol{i}}_{link} = (\hat{R})^{\mathrm{T}}\hat{\boldsymbol{i}}_{mesh} + \hat{M}\boldsymbol{i}_{ext}$ ($\hat{M}$ is the immediate generalization of matrix M defined above). The divergence and gradient operators are also generalized: $D \to \hat{D}$, $G \to \hat{G}$, and the expressions $\hat{D} = (\hat{G})^{\mathrm{T}}$, $\hat{R}\hat{G} = 0$ are still valid. The Biot–Savart equation now reads

$$\Phi_{ind;J} = \hat{\Lambda}\hat{\boldsymbol{i}}_{mesh} + \hat{\Delta}\boldsymbol{i}_{ext} \qquad \hat{\Lambda} \equiv (\Lambda\ \Lambda_{JS}) \tag{19}$$

where contributions coming both from Josephson-like and from superconducting currents are considered. As previously stated, the link currents are related to the mesh currents through

$$\begin{pmatrix} \boldsymbol{i}_{link;J} \\ \boldsymbol{i}_{link;S} \end{pmatrix} = \begin{pmatrix} R^{\mathrm{T}} & 0 \\ R_{JS}^{\mathrm{T}} & R_{SS}^{\mathrm{T}} \end{pmatrix}\begin{pmatrix} \boldsymbol{i}_{mesh;J} \\ \boldsymbol{i}_{mesh;S} \end{pmatrix} + \hat{M}\boldsymbol{i}_{ext}. \tag{20}$$

Zero magnetic flux inside grains implies $R_{SS}\phi_{link;S} = 0$. This, together with equation (20), gives $R_{SS}R_{JS}^{\mathrm{T}}\boldsymbol{i}_{mesh;J} = -R_{SS}R_{SS}^{\mathrm{T}}\boldsymbol{i}_{mesh;S}$; here, $\hat{M}$ has been defined in such a way that the curl of $\hat{M}\boldsymbol{i}_{ext}$ is null in the superconducting plaquettes (see figure 1). We can now re-express the Biot–Savart relation as

$$\Phi_{ind;J} = \tilde{\Lambda}\boldsymbol{i}_{mesh;J} + \hat{\Delta}\boldsymbol{i}_{ext} \qquad \tilde{\Lambda} \equiv \Lambda - \Lambda_{JS}(R_{SS}R_{SS}^{\mathrm{T}})^{-1}R_{SS}R_{JS}^{\mathrm{T}}. \tag{21}$$

The generalized Lagrangian is now

$$\begin{aligned} L(\hat{\phi}, \dot{\hat{\phi}}) = E_J\Big\{ & \cos\phi_J - \mathbf{1} + \frac{\beta_c}{2}\dot{\phi}_J^{\mathrm{T}}\dot{\phi}_J + (\boldsymbol{i}_{ext})^{\mathrm{T}}[(\hat{D}\hat{G})^{-1}\hat{D}]\hat{\phi} - \tilde{\boldsymbol{i}}^{\mathrm{T}}\phi_J - \frac{i}{2}(\phi_S)^{\mathrm{T}}\phi_S \\ & - \frac{1}{2}(\hat{R}\hat{\phi} + 2\pi\boldsymbol{f} + \hat{\Delta}\boldsymbol{i}_{ext})^{\mathrm{T}}\tilde{\Lambda}^{-1}(\hat{R}\hat{\phi} + 2\pi\boldsymbol{f} + \hat{\Delta}\boldsymbol{i}_{ext}) \\ & + \hat{\phi}\hat{R}^{\mathrm{T}}(\hat{R}\hat{R}^{\mathrm{T}})^{-1}\hat{R}\hat{M}\boldsymbol{i}_{ext}\Big\}. \end{aligned} \tag{22}$$

Equation (10) applied to (22) gives a set of Euler–Lagrange equations. On applying $\hat{D}$ to these equations, Kirchhoff expressions are obtained. The Biot–Savart law is then obtained by applying $(\hat{R}\hat{R}^{\mathrm{T}})^{-1}\hat{R}$. As $\phi_S = G_{SS}V$, $\Phi_S = 0$ is trivially obtained.

This procedure considerably increases the number of independent variables of the problem, and becomes highly CPU-time consuming. For a simplified version of the model, see, e.g., [27]

To conclude, we wish to point out that the forcing term, $i_{i;ext}$, may include both a dc component and an ac term, $i_{ac}\sin(\omega t)$. The presence of the latter opens up a vast field of research related to the competition between the frequency of the external forcing terms and the characteristic frequencies of the JJAs. In this review, however, we will restrict consideration to the case of an external dc force (the autonomous case). A description of the dynamics in the presence of an ac forcing term (the non-autonomous case) will be dealt with in a forthcoming paper [28]. Interesting contributions on this subject can be found in references [18, 29].

2.4. Comparison with other discrete models

Long junctions are usually described by means of the sine–Gordon equation. The phase-invariant gauge is a continuous function that varies along the junction $\phi(x)$, and obeys the equation [13]

$$\beta_c\ddot{\phi} - c\frac{\partial^2\phi}{\partial x^2} + \sin(\phi) = -\alpha\dot{\phi} + d\frac{\partial^2\dot{\phi}}{\partial x^2} - \gamma. \tag{23}$$

Here β_c is the McCumber parameter and $\alpha\dot{\phi}$ is the usual resistive term due to the tunnelling of normal electrons across the junction; the $d\,\partial^2\dot{\phi}/\partial x^2$ term accounts for the dissipation due to the flow of normal electrons parallel to the junction [30]; $\gamma = i/i_c$ is the usual bias term. If one neglects the third-derivative term and discretizes this model [31, 16], one obtains

$$\beta_c\ddot{\phi}_n + \alpha\dot{\phi}_n + i_n\sin(\phi_n) = i_{ext;n} + \frac{1}{w^2}\nabla^2\phi_n \tag{24}$$

where $\nabla^2\phi_n = 2\phi_n - \phi_{n-1} - \phi_{n+1}$ is the discrete Laplacian, and $w = D/\lambda_j$ is the discreteness parameter (D is the distance between points i and j, and λ_j is the junction penetration depth). The continuous model is obtained by making $h \to 0$.

An analogous model is obtained when considering 1D Josephson junction arrays, as shown in figure 3. In fact, conservation of the current at node i yields

$$\beta_c\ddot{\phi}_i + \dot{\phi}_i + \sin(\phi_i) = i_{ext} + i_i - i_{i-1}. \tag{25}$$

Here, the ϕ_i are the vertical gauge-invariant phases and i_i is the mesh current for cell i, as defined above. Along the superconducting horizontal links, the current density is given by

$$J_S = [(n_s e\bar{h})/m](\nabla\theta - (2\pi/\Phi_0)A)$$

(n_s is the superfluid density). Making the approximation that J_S is uniform, the (normalized) superconducting current is $i_S = \sigma J_S/I_c$ (σ is the cross-section of the current). Integrating the term $\nabla\theta$ along the border of plaquette i, one obtains

$$\oint(\nabla\theta)\,\mathrm{d}x = 2n\pi$$

which implies

$$2i_i = \frac{\sigma}{I_c D}\frac{n_s e\bar{h}}{m}(2n\pi - \phi_{i+1} + \phi_i - \Phi_i) \tag{26}$$

and thus

$$i_i - i_{i-1} = \frac{\sigma}{I_c D}\frac{n_s e\bar{h}}{2m}(\phi_{i+1} + \phi_{i-1} - 2\phi_i) + \Phi_{i-1} - \Phi_i + 2\pi(n_i - n_{i-1}). \tag{27}$$

If the array inductance is neglected and the external field is uniform ($\Phi_i = 2\pi f$), we obtain an equation which is formally equivalent to (24), with $w^2 = (I_c D/\sigma)2m/(n_s e\bar{h})$, plus an extra term taking into account the vortices existing in the array. Note that here the expression for w is strictly related to the characteristics of the supercurrent flowing in the horizontal branches, while that given in equation (24) derives from the discretization of the Josephson current, a procedure that has to be carried out for performing numerical simulations.

To include screening effects [32], one can proceed as follows. The mesh currents are linked to the flux across the plaquettes by $\Phi = \Lambda\boldsymbol{i}_{mesh} + \Delta\boldsymbol{i}_{ext}$. If the external current

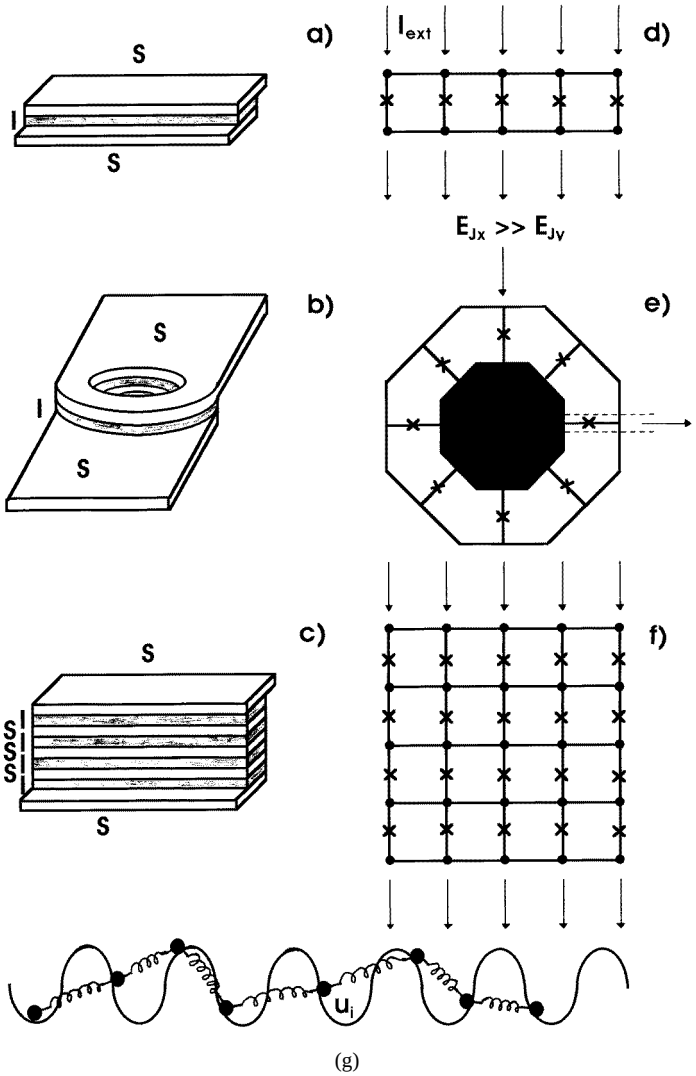

Figure 3. (a) A long Josephson junction; (b) a long Josephson junction ring; (c) a stacked junction; and their discrete counterparts: (d) an extremely anisotropic ladder (an inductively coupled 1D JJ chain); (e) an extremely anisotropic ring (i.e. a ladder with periodic boundary conditions); (f) an extremely anisotropic 2D array. The coupling along the x-branches (no junction) is much stronger than the coupling along the y-branches. (g) A schematic representation of a dynamical system described by the Frenkel–Kontorova equation.

is homogeneous, $\Delta_{p,j} i_{ext;j} = \xi_i i_{ext}$, where $\xi_i = \sum_j \Delta_{p,j}$, Now, on neglecting the non-diagonal terms of Λ, the magnetic flux is given by $\Phi_i = \Lambda_{0,0} i_i + \xi_i i_{ext} + 2\pi f$ and thus the current i_i is given by

$$(1 + \alpha\Lambda_{0,0}) i_i = \alpha(2n_i\pi + \phi_{i+1} - \phi_i) - \alpha\xi_i i_{ext} - \alpha\, 2\pi f \tag{28}$$

where

$$\alpha = \frac{\sigma}{I_c D} \frac{n_s e\bar{h}}{2m}.$$

The limit $\lambda \to \infty$ implies $\Lambda_{0,0} \to 0$, and equation (27) is obtained. However, when $\lambda_\perp$ is small enough that $\Lambda_{0,0} \geqslant 1$, the whole of equation (28) must be considered, and thus the current conservation at the ith node reads

$$\beta_c \ddot{\phi}_i + \dot{\phi}_i + \sin(\phi_i) = i_{ext}\left(1 - \frac{\alpha}{1+\alpha\Lambda_{0,0}}(\xi_i - \xi_{i-1})\right) + \frac{\alpha}{1+\alpha\Lambda_{0,0}}(2\pi(n_i - n_{i-1})) + \epsilon \tag{29}$$

where ϵ contains the contribution to the currents i_i, i_{i-1} coming from the fluxes across the rest of the plaquettes. Neglecting the non-diagonal components of Λ, again an equation formally equivalent to (24) is obtained, with $w = \sqrt{\Lambda_{0,0}}$; note that, in this particular system, $\lambda_j \propto \sqrt{\Lambda_{0,0}}$.

In all of the sine–Gordon-like equations considered above, w can be interpreted as a generic coupling strength of the vertical phases. The limit $w \to 0$ implies that $\phi_i \to \phi_{i+1}$; large values of a allow large horizontal variations of the phases.

In fact, the discrete sine–Gordon form is an approximate version of the equation of motion derived from the 'JJ array formalism', for when the phases vary slowly along the x-direction [33]. In fact, if one writes down the equations of motion (imposing Kirchhoff's law) for any pair of opposite nodes in the array $(\theta_{i,up}, \theta_{i,down})$, and subtracts them, one gets the following equation:

$$\left[1 - \left(\frac{C_x}{2C_y}\nabla^2\right)\right]\beta_c \frac{\mathrm{d}^2}{\mathrm{d}t^2}(\phi)_{n;y} + \left[1 - \left(\frac{R_y}{2R_x}\nabla^2\right)\right]\frac{2}{R_y}\frac{\mathrm{d}}{\mathrm{d}t}(\phi)_{n;y} + i_c \sin(\phi_{n;y}) - \frac{i_x}{2i_y}\sum_{i=\pm 1}\cos[\psi(n) - \psi(n+i)]\sin[\phi(n) - \phi(n+i)]/2 = i_{ext}. \tag{30}$$

Here, $\psi(i) = \theta_{i,up} + \theta_{i,down}$, and the ϕs are, as usual, the gauge-invariant phases along vertical links. Equation (30) becomes sine–Gordon-like if: (a) all of the combined space and time derivatives of order three or higher are negligible; and (b) the variation of θ along the x-axis is sufficiently slow that the cosine factor can be taken as 1, and the sine factor can be linearized:

$$\beta_c \frac{\mathrm{d}^2}{\mathrm{d}t^2}(\phi)_{n;y} + \alpha \frac{\mathrm{d}}{\mathrm{d}t}(\phi)_{n;y} + i_{n;y}\sin(\phi_{n;y}) - i_{ext} - \frac{i_x}{2i_y}\nabla^2(\phi)_{n;y} = 0. \tag{31}$$

The ∇^2 operator emerges in a natural way because of the coupling along the x-direction and because of the imposition of Kirchhoff's conservation law at the nodes.

On comparing equations (24) and (31) one immediately sees that in the latter the role of the discreteness factor is played by the coupling anisotropy of the array, $i_x/2i_y$. Indeed, for $i_x \gg i_y$, in order to keep the currents within reasonable limits, the horizontal phases must be small; their time derivatives $(\ddot{\phi}_x, \dot{\phi}_x)$ thus become negligible, and conditions (a) and (b) are fulfilled.

Thus the discrete sine–Gordon model, which describes systems of non-linear oscillators linearly coupled along the x-direction, is equivalent to the 'array formalism' in the limit of highly anisotropic JJ ladders.

It may also be of interest that if, in equation (30), one does not neglect all of the combined space and time derivatives, a term formally identical to the $\partial^2\dot{\phi}/\partial x^2$ present in equation (23) is obtained. Their physical meanings, however, do not coincide.

Let us now consider the Frenkel–Kontorova (FK) model. For a recent review on this model, see reference [34]. The FK model is used to describe systems composed of a set

of particles, interacting through a linear force, placed in a periodic potential; see figure 3, where, as an example, the 1D case is shown. The Hamiltonian is

$$H = \sum_{i,j}\{V(u_i) + U(\Delta u_{ij})\} = \sum_{i,j}\left\{\frac{K}{(2\pi)^2}[1 - \cos(2\pi u_i)] + \frac{1}{2}(\Delta u_{ij})^2\right\} \tag{32}$$

where u is the position of the ith particle and the sum over j is over first-nearest neighbours; K gives the amplitude of the periodic potential. The FK model applies to systems of particles whose number is not constrained to be equal to the number of potential minima; it can be either larger or smaller. In order to apply the FK model to the case of the JJ ladder we have to identify the positions of the particles with the gauge-invariant phases of the JJs lying along the y-direction, $\phi_{i;y}$. As a consequence, the number of minima of the periodic potential is fixed and equal to the number of $\phi_{i;y}$ minus one. If one also adds a dissipative and a kinetic term, the FK model can be straightforwardly mapped onto the discrete sine–Gordon one.

2.5. 'Particle' versus phase dynamics

In the introduction we pointed out the strong correlation between the operational mode of cryodevices based on JJAs and the dynamics of vortices. We have shown that a complete description of the JJA dynamics can be given in terms of the gauge-invariant phases. To conclude this section and, also, the part of the review devoted to the 'JJ array formalism', we would like to discuss the relationship that exists between the vortex and phase descriptions of JJA dynamics.

In a very general manner, a vortex can be treated as a particle [38, 39] that, under the action of a certain potential, $V(x)$, is forced to move in a viscous medium. Periodically it has to overcome energy barriers related to the links encountered along its trajectory.

When we consider the dynamics of a single vortex, the potential $V(x)$ can be identified with its Gibbs energy, $U(x)$. This latter can be decomposed into six terms [35, 36]: the core energy $U_c = \pi^2/2$, defined as half the energy needed to create a vortex–antivortex pair; the energy of a vortex in the absence of magnetic fields and external currents, $U_0(x)$; the energies due to the interactions with the external field and with the bias current, $U_f(x)$ and $U_i(x)$; the term that takes into account the periodicity of the array, $U_{pot}(x)$; and $U_{mag}(x)$, the term due to the screening currents. Strictly speaking, U depends also on the vertical coordinate, y. Here, in order to simplify the discussion, we assume that the vortex moves along the central row of the array ($y = 0$). The analytic expressions for $U_i(x)$, $U_f(x)$, $U_{pot}(x)$ and $U_{mag}(x)$ in terms of $\overline{h}I_c/(2e)$, with x normalized to a, are given by

$$U_i(x) = -2\pi \mathrm{i}\left(x + \frac{L}{2}\right) \tag{33}$$

$$U_f(x) = -\frac{\pi^2 L^2}{2} f\left(1 - 4\left(\frac{x}{L}\right)^2\right) \tag{34}$$

$$U_{pot}(x) = -\frac{1}{2}E_B \cos(2\pi x). \tag{35}$$

$$U_{mag}(x) = \frac{1}{2}(\boldsymbol{i}_{link})^{\mathrm{T}} \frac{1}{4\pi\lambda_\perp} \mathrm{ff}\, \boldsymbol{i}_{link} = \frac{1}{2}\boldsymbol{a}^{\mathrm{T}}\, 4\pi\lambda_\perp \mathrm{ff}^{-1}\boldsymbol{a}. \tag{36}$$

where: L is the array dimension in the direction perpendicular to the flow of the bias current; the coordinates are normalized to the cell dimension a; and E_B is the energy barrier that the vortex must overcome to move from one cell to the next one. We fixed the origin of the coordinates, $x = 0$, at the central column of the array.

As far as $U_0(x)$ is concerned, its expression for finite samples and $\lambda_\perp = \infty$ is

$$U_0(x) = \pi \ln\left(\frac{2L}{\pi}\cos\left(\frac{\pi x}{L}\right)\right). \tag{37}$$

The modification of $U_0(x)$ for finite value of $\lambda_\perp$ [36] is discussed in the next section.

Given the above expression, the equation of motion for the vortex can be written in the following way:

$$M_v l_a \ddot{x} = -\frac{E_J}{l_a}\frac{\mathrm{d}U}{\mathrm{d}x} - \eta l_a \dot{x} \Rightarrow M_v l_a \ddot{x} + \eta l_a \dot{x} + \frac{E_J}{l_a}\left(\pi E_B \sin(2\pi x) - 2\pi \mathrm{i} + 4\pi^2 f x + \frac{\mathrm{d}U_0}{\mathrm{d}x} + \frac{\mathrm{d}U_{magn}}{\mathrm{d}x}\right) = 0 \tag{38}$$

where η is the coefficient of viscosity. The equation of motion of the particle (vortex), thus, resembles very much that of the phase of a single JJ subjected to a washboard potential.

It is natural to associate the kinetic term $(1/2)C\sum_{ij} V_{ij}^2$ with $(1/2)M_v\dot{x}^2$. In zero magnetic field and in the no-screening approximation, the phase profile of the phases around a vortex is given by [37] $\phi = \arctan[(y_i - y_0)/(x_i - x_0)]$. In the quasi-static limit one obtains [23] $V_{ij} = (\Phi_0/2\pi)(\dot{x}/l_a)(\phi_i - \phi_j)$ and, by summing over the phases, one arrives at, in agreement with reference [39], the following mass expression:

$$M_v = \frac{{\Phi_0}^2 C}{2l_a^2}. \tag{39}$$

On the other hand, the power dissipated by the moving vortex is equal to the sum of the power dissipated in all of the links of the array, $\eta u^2 = \sum_{ij} {V_{ij}}^2/R_{ij}$. η can be expressed in terms of the effective shunt resistance r_e (i.e. the equivalent resistance of the whole circuit between two sites i and j) [40]:

$$\eta = \frac{{\Phi_0}^2}{2\,l_a^2 r_e}. \tag{40}$$

Now, if in equation (38) one makes the substitution $2\pi x \to \phi$, one obtains, in the limit of very large samples ($L \to \infty$), the following expression:

$$\frac{{\Phi_0}^2}{2\pi^2}\frac{C}{2}\ddot{\phi} + \frac{{\Phi_0}^2}{2\pi^2}\frac{1}{2r_e}\dot{\phi} + E_J(E_B \sin\phi - 2i) = 0 \tag{41}$$

which shows the equivalence between phase and 'particle' dynamics in the limit of large samples and for $f \to 0$. Indeed, only in these limits are U_{magn} and U_0 independent of x in the bulk of the array (i.e. at a distance from the border larger than the vortex size) and is the 'arctangent' expression applicable. From equation (41) it emerges that the depinning current of the array is $i_d = E_B/2$. We can define vortex-like quantities analogous to the junction-like ones β_c and $\omega_p = \sqrt{\beta_c}/(RC)$ (the plasma frequency) by $\beta_{cv} = E_B\beta_c$ and $\omega_{pv} = \sqrt{E_B}\omega_p$.

Finally, one should note that equation (39) implies no dependence of M on screening and, also, a linear dependence of M on C, while equation (40) implies a constant η if, like in the Bardeen–Stephens model, r_e is taken as constant. However, strong deviations from the behaviour predicted by equation (39) and (40) have been 'observed' [41, 47, 36, 42] in both overdamped and underdamped junctions and these will be discussed in the next section.

3. The dynamics of massless vortices

When $\beta_c < 1$ the dynamics is overdamped. In the extreme limit, when $C \to 0$, the vortices can be considered massless 'particles'. An example of arrays made up of superconducting junctions having a capacitance close to zero is that of SNS arrays; see figure 1. In these systems the coupling to the environment is very strong, ohmic dissipation dominates the dynamics and the motion of the vortex is *viscous*; under the assumption of a Bardeen–Stephens-like dissipation mechanism, equation (38) reduces to

$$\eta v = -\mathrm{d}U/\mathrm{d}x. \tag{42}$$

Since the main goal of this review is to describe single-vortex dynamics (i.e. the kink dynamics) in discrete systems, we will go through the discussion of the conditions needed to form and depin a vortex, and the experimental parameters that have the major influence on the characteristics of the vortex motion (energy barriers, viscosity, bias current etc) and which, in turn, define the vortex velocity. Particular attention will be paid to pointing out the effect of screening currents and the sample geometry.

3.1. The pinning potential and depinning current

As is well known, the Kosterlitz–Thouless–Berezinskii (KTB) critical transition [43] separates the resistive regime of the array (at high temperatures) from its superconductive one (at low temperatures).

Below the critical temperature ($T_{KTB} \approx E_J/K_B$), in the absence of an external magnetic field, vortices are bound in vortex–antivortex pairs. In the absence of energy barriers, such as in a continuous superconducting film, any non-zero current will break the most weakly bound pairs. In discrete systems like the arrays, however, each link represents a barrier to the vortex motion and vortex–antivortex pairs remain bound for bias currents lower than a given value I_d. Indeed, if the energy supplied by the external source in the time unit is not high enough to break these pairs, the array remains in a superconductive regime: no free vortices are present and no voltage is measured at the sample edge. I_d is usually referred to as the depinning current.

In the presence of a magnetic field, unpaired vortices are present for temperature lower than T_{KTB}; in fact the field induces a 'torque' on the phases, ϕ, and when it is high enough (i.e. when the sum of the phase differences along the contour of the sample is $>2\pi$) a vortex will enter the array in order to minimize the energy of the system. These vortices, however, although unpaired, are pinned: in order to pass from one cell to the next, they must overcome the energy barrier E_B, also known as the vortex pinning potential. Thus, the vortex/antivortex remains pinned in a plaquette until it receives enough energy to jump over the barrier, from either thermal noise (temperatures must be such that $k_B T > E_B$), or the bias current. When $T < E_B/k_B$, and the current is lower than the *depinning current*, $I_d(T)$, the vortices are not able to move and no voltage is measured.

Numerical simulations show that in 2D arrays a static configuration with one single vortex can be stabilized also in the absence of any frustration (internal or external); it is worthwhile to stress that only in this case are the phases expected to follow the 'arctangent' distribution [37]. The same is not true for the ladder, for which a vortex can be stabilized only for $f > 0.12$ or $\lambda_\perp < 2$ [44]. By taking the energy difference between the case in which the vortex is centred in a cell and that of a vortex centred on a junction, one can determine the static E_B [37].

In the no-screening limit, $\lambda_\perp = \infty$, it has been found that the static value of E_B, in terms of E_J, is 0.2 for a 2D square array and 0.043 for a 2D triangular array. These values have

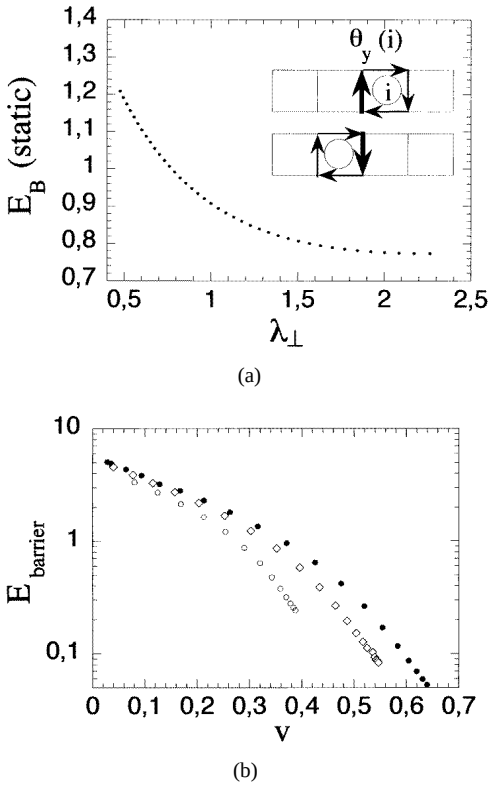

Figure 4. (a) A ladder: E_B (static determination) versus $\lambda_\perp$; in the inset we show the current distribution around a vortex when it is in cells i and $i-1$. (b) A ladder: E_B (dynamic determination) versus the vortex velocity for different values of $\lambda_\perp$; the three curves have been obtained with different values of i_{dc}: 0.8 (○); 0.9 (◇); 0.95 (●). (c) An anisotropic ladder, 32×2: E_B (dynamic determination) versus E_{Jx}/E_{Jy} for $\lambda_\perp = 10$ for the different values of i_{dc} given in the key. (d) is as (c) but with $\lambda_\perp = 1$.

been worked out for the limit of very large arrays [37] and have been confirmed by numerical simulations of the dynamics in a small array with periodic boundary conditions [45].

These values of E_B are substantially affected by decreasing $\lambda_\perp$. For example, at $\lambda_\perp = 1$, E_B is greater than 0.4 [17].

It has been noted that finite-size effects may also affect the value of E_B; it increases with decreasing array size [46]. This observation for triangular JJAs agrees with calculations performed for the ladder [47], where it was found to be much higher than in the 2D case. In fact, in the region of stability of the single-vortex solution, one always finds $E_B > 0.75$ and even $E_B \approx 1.2$ for $\lambda_\perp = 0.5$; see figure 4.

In extremely anisotropic ladders [32] E_B becomes negligible for $\lambda_\perp > 1$, a result found in recent simulations of the dynamical properties of anisotropic ladders, performed as a function of the coupling anisotropy, E_{Jx}/E_{Jy}: $E_B \to 0$ for $\lambda_\perp > 1$ and $E_{Jx}/E_{Jy} > 5$. On the other hand, for $\lambda_\perp \leqslant 1$ and $E_{Jx}/E_{Jy} > 10$–100, E_B saturates and the saturation value strongly depends on $\lambda_\perp$ and i_{dc} [28].

Experimentally, it is possible to measure E_B by measuring I_d. In fact, in the limit of a very large array, I_d should be equal to $E_B/2$; see equation (41). The measurements on both 2D square and triangular arrays give values somewhat higher than the numerical predictions

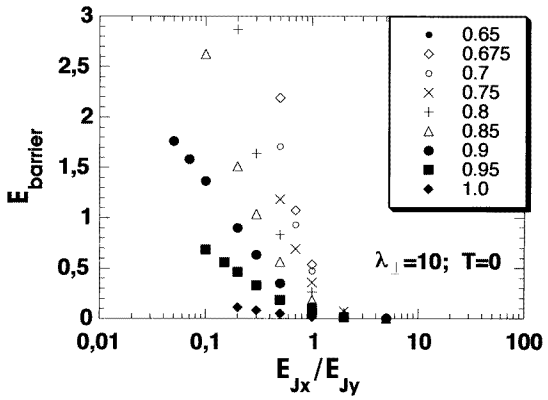

(c)

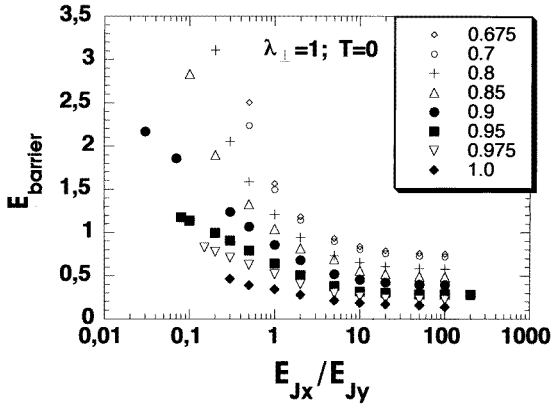

(d)

Figure 4. (Continued)

[22]. The discrepancy may be due to pinning and/or to the finite value of $\lambda_\perp$ (the measured sample had 300 plaquettes to a side, while $\lambda_\perp = 10$).

We do not know of any experimental measurement of I_d for a standard overdamped ladder. Accurate measurements of I_d versus $\lambda_\perp$, on the other hand, have been obtained for extremely anisotropic (underdamped) ladders subjected to a small, $f = 0.2$, magnetic field (see reference [48]) and, also, for a single underdamped ladder as a function of f [49].

Finally, we would like to point out that I_d can be modulated [48] by the application of an external magnetic field, f, and that its value increases as $I_d \approx 0.1[1 + \pi\delta f]$ in the presence of 'moderate' lattice defects [50]; δ gives a measure of the strength with which defects tend to pin the vortex.

3.2. The vortex velocity and the dynamical determination of E_B

E_B depends not only on $\lambda_\perp$, but also on other factors such as the bias current and the sample geometry. E_B can be determined dynamically from the variation of the array energy, $\Delta U(\tau)$, induced by the vortex motion as a function of the time. By decomposing $U(\tau)$ one can extract U_{pot} [47] and thus E_B; see the previous section.

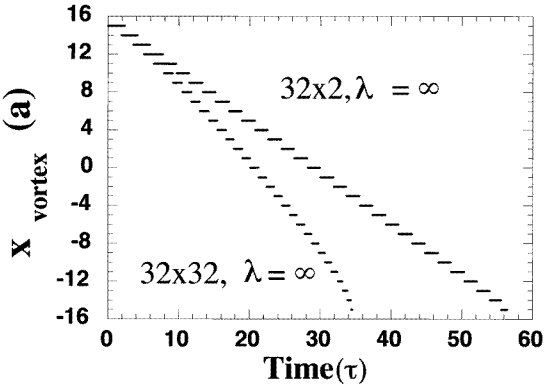

(a)

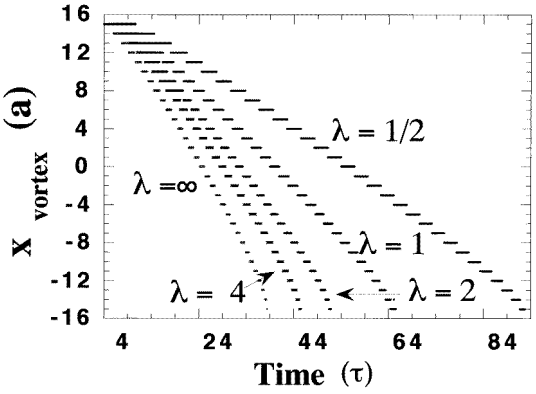

(b)

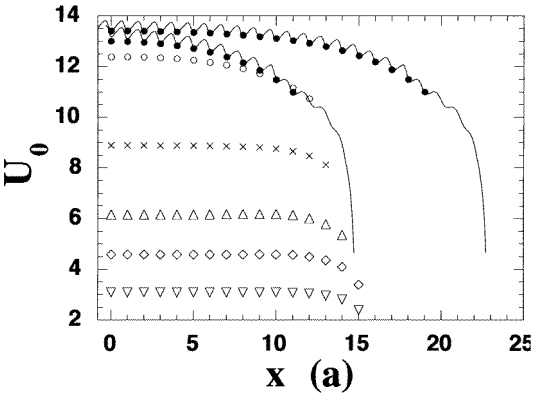

(c)

Figure 5. (a) Examples of vortex trajectories as functions of the lattice size. (b) Examples of vortex trajectories as functions of $\lambda_\perp$ for a 32×2 ladder. $i_{dc} = 0.9$. (c) $U_0(x)$ for a 32×32 array, for different values of $\lambda_\perp$: 1/2 (∇); 1 ($\diamond$); 2 ($\triangle$); 32 ($\times$); 64 ($\circ$). For a 32×32 and a 48×32 array we also compare a dynamical determination of $U_0(x)$ (solid lines) with the static one when $\lambda_\perp = \infty$.

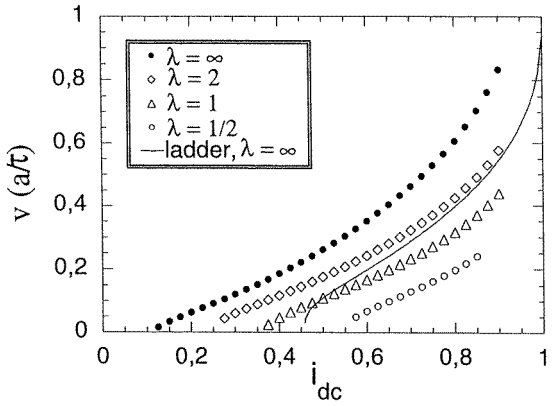

(a)

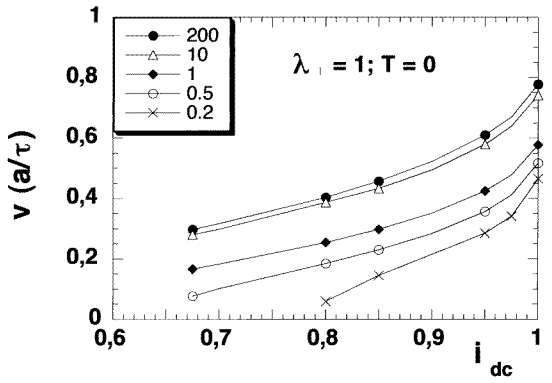

(b)

Figure 6. (a) A 2D array: the steady-state vortex velocity, v, versus i_{dc} for different values of $\lambda_\perp$: ∞ (•); 2 (◊); 1 (△); 1/2 (○). Comparison is made with the results obtained for a ladder in the absence of inductance (the continuous line). (b) An anisotropic ladder: v versus i_{dc} for different values of the ratio E_{Jx}/E_{Jy}; see the key.

It is worth mentioning that to study the single-vortex dynamics one does not need necessarily to stabilize the vortex by applying a small magnetic field that has the effect of applying a continuous perturbation to the system. Indeed, the creation of a single vortex can also be achieved by temporarily breaking a vertical link [51, 52]. For sufficiently large currents, vortex/antivortex pairs are created at the edge of the defect. By breaking the rightmost link, it is possible to induce the creation of just one vortex at the border of the ladder. After its creation, the vortex, subjected to the Lorentz force, moves along the ladder in an environment free of any perturbation due to external magnetic field. The vortex velocity can be calculated directly from its trajectory.

The results obtained for a ladder, by applying this procedure, are displayed in figures 5 and 6 and can be summarized as follows.

(a) The vortex moves with a constant velocity; acceleration occurs only when it crosses the outermost cells. This constant-velocity propagation is observed regardless of what the values of i_{dc} and $\lambda_\perp$ are.

(b) The vortex velocity increases almost linearly with i_{dc} for $i_{dc} < 0.75$ and superlinearly

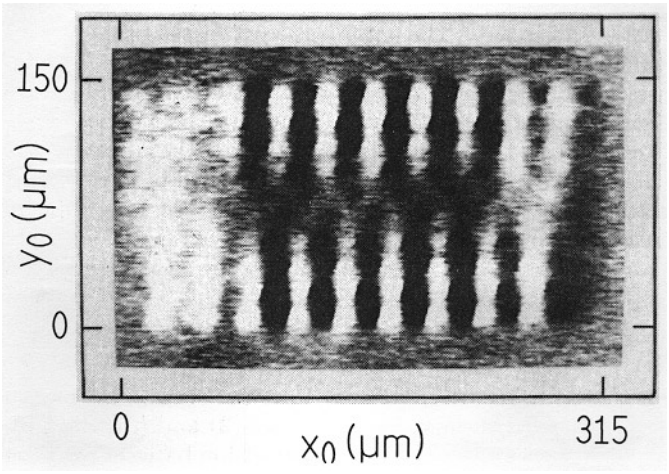

(a)

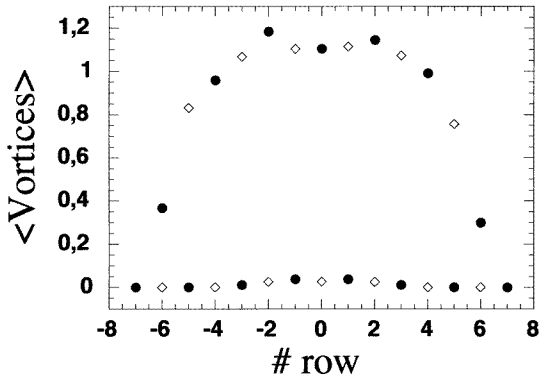

(b)

Figure 7. Alternate-vortex motion (AVM) imaged by LTSEM. (a) A grey-scale representation of the voltage image $\Delta V(x, y)$ for a 20×10 array at $T \approx 5$ K. I_{dc} flows horizontally through the array; white (black) signals at the top indicate incoming vortices (antivortices); on the same row, black (white) signals at the bottom indicate outgoing vortices (antivortices). (b) AVM: the time-averaged number of moving vortices (•) and antivortices (◇) worked out by means of numerical simulations. Note that, like for the real experiment, the AVM is disturbed by edge effects. (c) The variation of the voltage signal expected on the basis of the simple model described in reference [53]. (d) The measured ΔV profile on a single row of a 10×10 array. (e) The variation of the Josephson energy induced by the moving vortex as detected by numerical simulations; the vortex has been generated at the 12th plaquette. *(a), (c) and (d) are courtesy of Doderer and co-workers [53].*

for higher currents; v decreases with $\lambda_\perp$.

(c) E_B decreases with increasing vortex velocity. For $\lambda_\perp = \infty$, $E_B(v)$ follows a simple exponential dependence, $E_B = \alpha \exp(-\beta v)$ where $\alpha \approx 2.5$ and $\beta \approx 2\pi$. For a finite $\lambda_\perp$, $E_B(v)$ does not follow any simple functional behaviour.

(d) As expected, the limiting expression for the 2D U_0 is not applicable to the case of a ladder.

For 2D square arrays the situation is quite different.

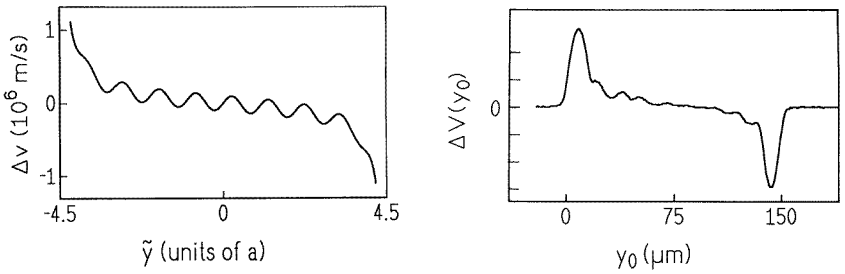

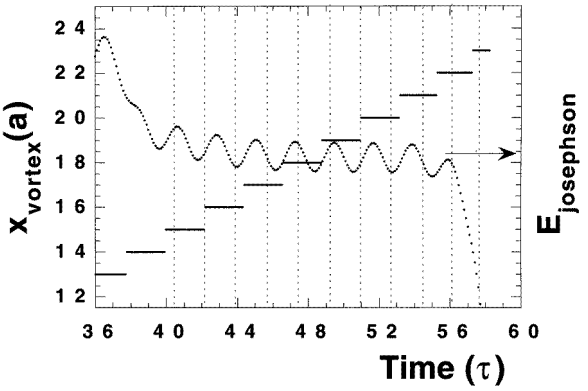

Figure 7. (Continued)

(a) The acceleration rate grows with the vertical extent of the array and with decreasing $\lambda_\perp$. Uniform linear motion is observed only when the vortex moves in the central zone of a large array, far from the edges.

(b) In the central zone the vortex velocity increases with the bias current and with the vertical length of the array, and decreases with decreasing $\lambda_\perp$.

(c) E_B is a decreasing non-trivial function of the vortex velocity.

(d) The expression for U_0 valid for $\lambda_\perp = \infty$ is modified by screening: the average value of U_0 decreases with $\lambda_\perp$ and the spatial dependence of U_0 flattens.

(e) Above a certain value of the bias current (which depends on $\lambda_\perp$ and on the vertical size of the array) the annihilation of a vortex (antivortex) at the border of the array induces the creation of new antivortices (vortices) in the adjacent rows, leading, over time, to the formation of a new dynamical state: the so-called alternate-vortex motion, AVM.

This state was first described by Lachenmann *et al* [53] on the basis of their LTSEM observations, and confirmed in numerical simulations [54]. The AVM—see figure 7—consists in an ensemble of vortices/antivortices that are reflected up and down by the even/odd (or vice versa) rows of the array. In LTSEM measurements, by means of a scanning electron beam, one locally perturbs the sample dynamics and detects an induced voltage variation, $\Delta V(x, y)$, at the border of the array. $\Delta V(x, y)$ is proportional to the derivative of U (see figure 7) and thus to the vortex velocity (more on the basic principles of the LTSEM imaging is reported in reference [55]). The LTSEM trace of figure 7 confirms the acceleration of the vortex in the proximity of the array edges. The smoothing of the

sinusoidal oscillations of the LTSEM signal in the centre of the array has been ascribed to the variation of the vortex velocity profile induced by the electron beam; however, since the LTSEM results are average measurements of the dynamical state of the sample, vortex/antivortex recombinations (which are allowed under certain conditions) may also contribute.

It is important to note that, provided that the bias current is high enough, the existence of an initial vortex (or any other symmetry-breaking mechanism—such as screening [56]) is a sufficient condition for the development of AVM [36].

A bridge towards the continuous limit is provided by the study of vortex dynamics in overdamped anisotropic systems. Up to now only preliminary studies on anisotropic ladders have been available [28]; their findings can be summarized as follows:

(a) no matter what the value of E_{Jx}/E_{Jy} is, the vortices always annihilate at the edge of the array;

(b) v increases with E_{Jx}/E_{Jy} and saturates, but only for $\lambda_\perp \leqslant 1$; and

(c) for a sufficiently high i_{dc} and a sufficiently low anisotropy, dynamical instabilities are observed.

Many of the above observations find a common explanation in the dependence of the vortex size on $\lambda_\perp$ and on the array geometry; see the next section.

3.3. Energy dissipation, the viscous coefficient and the vortex dimension

The value of the viscosity coefficient η can be calculated by measuring v and the dissipated power, $W_{diss} = \mathrm{d}E_{diss}/\mathrm{d}t$; v can be obtained from the vortex trajectory, and W_{diss} is just $[\Phi_0^2/(4\pi^2)]\sum_{ij}\dot{\phi}_{ij}^2/R_{ij}$. r_e is not constant but depends on $\lambda_\perp$ and the array geometry, a dependence that can be understood by considering the vortex size [47, 36].

In figure 8 we show the spatial distribution of the cell currents, measured in different situations and for different samples. We can summarize the results as follows: the vortex size increases with

(a) $\lambda_\perp$ (see for example the static determination for a ladder);

(b) the vertical size of the array; and

(c) the anisotropy.

In addition, we observe the development of an asymmetry in the vortex profile (i.e. a higher current density towards the back of the vortex) which is caused by

(a) the superlinear increase of v with i_{dc};

(b) the vertical extent of the array; and

(c) the coupling anisotropy.

An increase of the vortex velocity, and thus of the equivalent resistance, is always associated with an increase in the vortex size. This is a quite reasonable result because r_e is defined roughly as the dimension of the sub-array over which the vortex extends. The larger r_e, the smaller the damping coefficient η, and the higher the velocity.

In overdamped arrays, thus, η cannot be assumed constant, but depends on the bias current, on the screening and on the geometry of the array.

Our results are in agreement with those reported in reference [41], where to account for the dependence of η on the bias current the following phenomenological law has been suggested: $\eta = A/(1 + B\dot{x})$ with $A = 2.67$ and $B = 1.80$.

A dependence of η on $\lambda_\perp$ has been found and discussed also in reference [42], where, assuming a linearized Josephson current equation, the authors worked out the following

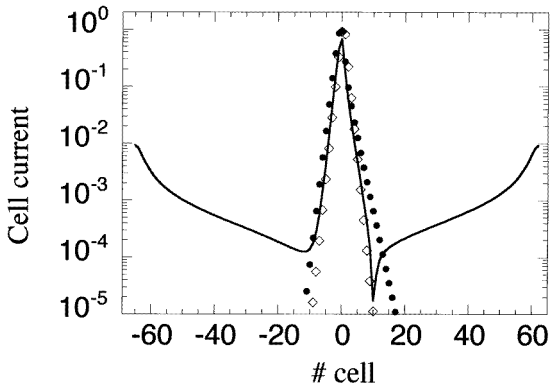

(a)

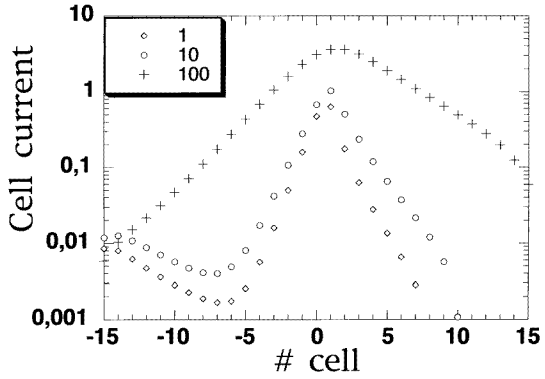

(b)

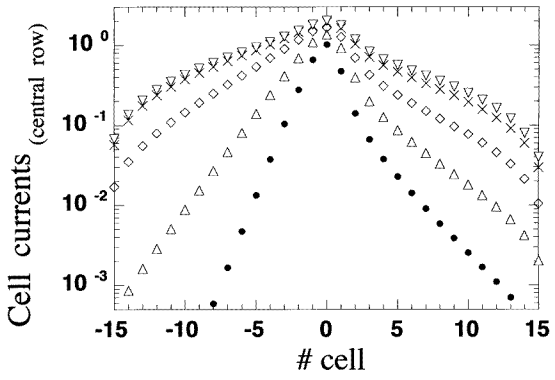

(c)

Figure 8. (a) An 128-cell ladder: the shape of a moving vortex in the cases where $i_{dc} = 0.9$, $\lambda_\perp = \infty$ (•), $i_{dc} = 0.5$, $\lambda_\perp = \infty$ (◊) and $i_{dc} = 0.9$, $\lambda_\perp = 1$ (continuous line). The asymmetry of the distribution is due to the fact that the vortex is in motion (from right to left). (b) An anisotropic ladder: the shape of a moving vortex as a function of E_{Jx}/E_{Jy}; see the key. (c) A 2D array: the shape of a moving vortex as a function of the transverse size of the array for $32 \times N_y$ arrays ($N_y = 2$ (•), 4 (△), 8 (◊), 16 (×) and 32 (▽)).

relation:

$$\eta = \frac{{\Phi_0}^2}{2l_a^2 r_n} G(\lambda_\perp)$$

where r_n is the normal junction resistance and

$$G(\lambda_\perp) \approx 1 - \frac{1}{2}\sqrt{\frac{2}{\pi}}\frac{1}{\lambda_\perp} + \frac{7 + 3\ln(8\pi\lambda_\perp^2)}{48\pi}\frac{1}{\lambda_\perp^2}.$$

This expression provides a good fit to the data but does not include the well known dependence of η on the bias current.

One may note, however, that none of the above expressions take into account the dependence of η on the size of the array (i.e. on the size of the vortex) in the y-direction. Further investigations on this subject are still needed.

E_B, also, decreases with the vortex size. The fact that a less localized particle should overcome a lower energy barrier is also a reasonable result: the larger the vortex is, the smoother its shape becomes; thus the crossing from one cell to the next one requires less dramatic phase shifts and, thus, a smaller energy.

The dependence of the extent of the vortex on the vertical size of the array also modifies the profile of $U_0(x)$—see figure 5—and explains the acceleration to which the vortex is subjected in the proximity of the borders. On decreasing $\lambda_\perp$, the vortex becomes more localized, U_0 flattens and the region in which the vortex moves with a constant velocity enlarges.

It is interesting to note that in the anisotropic ladders, for short $\lambda_\perp$ ($\lambda_\perp \approx 1$) the vortex cannot extend beyond a certain limit and, as a consequence, for $J_x/J_y > 50$–100, v saturates.

Let us now consider the asymmetry of the vortex shape. Such an asymmetry decreases with $\lambda_\perp$ and increases with v, becoming more visible when v starts to increase superlinearly with i_{dc}. It is likely that the asymmetry develops when the transit time of the vortex, l_a/v, becomes shorter than a certain characteristic restoring time of the array.

The distortion of the vortex seems to be evidence for a non-canonical dissipation mechanism. When the vortex moves too fast, the phases have no time to relax; the system is not able to dissipate all of the injected energy and an amount of energy is stored in the array in the form of a more or less extended perturbation of the phases (since here we are dealing with overdamped arrays, it is not obvious that these perturbations would travel).

Such a non-canonical dissipation mechanism may explain the vortex 'reflection' and the development of the AVM in 2D arrays. In fact, at the moment of the vortex annihilation it may be that the energy stored in the sample is large enough to induce the formation of new vortices/antivortices that propagate in the opposite direction. If the number of induced vortices/antivortices becomes larger than the number of annihilated ones, the energy stored in the array progressively increases and the process continues until the AVM, a steady dynamical state, is fully developed.

To conclude this section, we would like to point out that experiments intended to study in detail the true single-vortex dynamics (not the average dynamical state of the array) are possible [57], but since the measurements are quite 'delicate' ones, they would require a coordination of many groups and resources [58] that, unfortunately, up to now has not been made possible.

4. Dynamics of massive vortices: underdamped JJAs

When the junction capacitance is not negligible, $\beta_c \neq 0$, the vortex acquires a mass. When β_c is somewhat greater than unity, the vortex motion enters the underdamped regime. Usually, information on the average vortex dynamics in underdamped arrays can be obtained by measuring the I–V characteristics, which provide evidence of the existence of different dynamical regimes. One can distinguish between:

(i) a low-voltage regime in which one can observe *zero-field steps* [59] when $f = 0$ (induced by the back-and-forth motion of vortices reflected at the boundaries); *flux flow* (induced by the motion of vortices that are continuously injected at one edge and annihilated at the opposite one) and *Fiske steps* (due to the resonance between the moving vortex and the waves excited in its wake), when $f \neq 0$, in both the linear [69] and non-linear regimes [59, 63];

(ii) a high-voltage regime where instabilities show up: a whirling mode in extremely anisotropic ladders (i.e. 1D parallel arrays) and row switching in 2D arrays; the latter are observed when $f \neq 0$ or $\lambda_\perp \neq \infty$; and

(iii) a linear branch regime where V increases linearly with I.

Thanks to numerical simulations, one can investigate the details of the vortex motion in all of the above regimes. In the following we will give an updated overview of our present understanding of single-vortex dynamics in underdamped arrays.

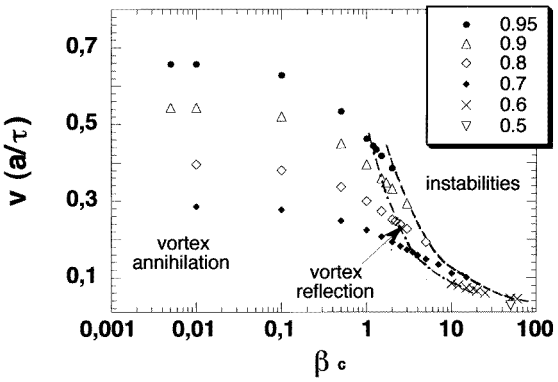

Figure 9. The steady-state velocity versus β_c in the case of a massive vortex in a 2×32 ladder for different values of i_{dc}; see the key. The lines indicate the borders between the different dynamical regions where one observes vortex annihilation, vortex reflection and dynamical instabilities.

4.1. Vortex depinning, vortex annihilation and vortex reflection

When β_c takes a value somewhat higher than 1:

(a) the I–V characteristic becomes hysteretic [22]—this observation supports a 'particle-like' description of the vortex dynamics;

(b) the vortex retrapping current is lower than the depinning current, but, due to thermal fluctuations, the difference is reduced progressively to zero for more and more resistive samples; and

(c) the depinning current decreases with increasing β_c. In reference [60] it is suggested that i_d should decrease as $\sqrt{\beta_{v,c}}$, a prediction that when compared with the experimental results of reference [22] shows a reasonable agreement, despite the large spread of the parameter values ($\lambda_\perp$ and the geometrical size) of the samples considered.

The vortex motion is influenced by parameters like β_c, i_{dc} and $\lambda_\perp$ also in underdamped arrays. As an example, in figure 9 we show, for the case of a ladder with $\lambda_\perp = \infty$, a v versus β_c plot. The lines separate different dynamical regimes. In the 'annihilation' regime the motion of the vortex turns out to be very similar to that observed in the massless case. Again v depends on i_{dc} but, in addition, in underdamped arrays v decreases with β_c and tends to be independent of i_{dc} for very large β_c.

Annihilation of vortices at the borders is observed also when an external magnetic field f is switched on. Vortices are continuously generated at one border and annihilate at the opposite one. As a consequence, a non-zero voltage is measured: this is the so-called flux-flow regime. The flux-flow resistance, r_{ff}, characteristic of this regime, can be shown, under certain approximations, to be linearly proportional to both f and r_e. The linear dependence of r_{ff} on f (up to $f \approx 0.25$) has been checked both experimentally [22] and numerically [41]. To check the proportionality between r_{ff} and r_e one has to take into consideration the fact that, as for the overdamped arrays, r_e depends on the size of the vortex and thus cannot be identified straightforwardly with the normal-state resistance of the junctions. An experimental proof of this is reported in reference [42].

When β_c is high enough, one observes a transition to a new dynamical regime: that of 'vortex reflection' at the borders. At each reflection the vortex/antivortex is reflected into an antivortex/vortex; note that in underdamped systems we are faced with a true vortex reflection: the incident and the reflected 'particle' move on the same row. The vortex reflection occurs not only in 2D arrays [61] but also in ladders [28] (where massless vortices always annihilate at the borders) and in extremely anisotropic ladders [59, 70]. Vortex reflections may be repeated at each border, being analogous to the 'soliton' reflections in continuous long Josephson junctions, LJJs [15]; in a very similar manner, such reflections produce a non-zero average voltage, i.e. a zero-field step. In 2D JJAs the zero-field step seems to be characterized by a relevant non-zero slope [61], but it is likely that in anisotropic arrays with a short $\lambda_\perp$ the zero-field step would flatten. This is a point that has to be checked.

Also, for underdamped arrays we expect η and the vortex mass to depend on $\lambda_\perp$ and the vertical extent of the array, i.e. on the vortex size. Some experiments and numerical checks, although not complete, can be found in reference [42].

When β_c is of the order of 50 or more and $\lambda_\perp$ is not lower than 5, the region of the β_c versus i_{dc} plot in which one observes vortex reflection splits into two and an additional vortex annihilation area materializes in between [61]. It is suggested that this latter is caused by the excitation of additional dissipative modes (see the next section) that interfere with the vortex motion, slow it down and cause its annihilation.

Preliminary results seem to indicate that no such additional vortex annihilation region exists in the underdamped ladder, an observation that agrees with the progressive shrinking of the 'reflection' region in 2D arrays with decreasing $\lambda_\perp$ (at least when β_c takes values as high as 100) [28]. This point also needs further investigation.

4.2. Dissipation and resonances

In the flux-flow regime it is observed that for $\beta_c > 1$, r_e decreases as $\sqrt{\beta_c}$ and takes values even smaller than the normal resistance. In agreement with experimental observations [22], numerical calculation shows that η_c increases as $\approx \eta\sqrt{\beta_c} = 2\pi E_j/a^2\omega_p$ (a relationship

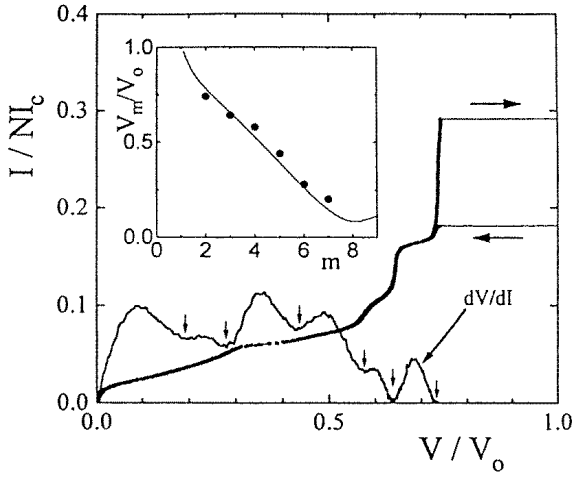

Figure 10. The experimental I–V curve for one vortex trapped in the ring measured at 6.4 K, where $\Lambda_j^2 = 2.2$ and $\beta_c = 61$. The solid line shows $\mathrm{d}V/\mathrm{d}I$. Inset: the voltage position of the six steps versus the mode number m. The curve is a fit to the dispersion relation given by van der Zant *et al.* The sample used in the experiment is sketched in figure 3. *Courtesy of van der Zant et al [63].*

strictly correct only if v increases linearly with i_{dc}); that is, η_c does not depend on r_e [60]. These results are not compatible with Bardeen–Stephens-like ohmic dissipation [62] and suggest the existence of an additional dissipation mechanism [22]. The existence of this latter also defines the limits of the calculation of the vortex mass, as derived in the previous section. The cause of the additional dissipation mechanism has been identified as the excitation of spin waves in the wake of the moving vortex [45, 60]. Such a hypothesis has been proved correct in numerical simulations either by the direct numerical observation of current oscillations or by the appearance of resonances in the I–V characteristics in linear and non-linear regimes (Fiske steps). In particular, these latter have been experimentally measured in an extremely anisotropic ring (figure 10) [63] and ladder [65, 70], and predicted by several groups [64, 31, 65] on the basis of discrete sine–Gordon-like equations.

The experimental observations confirm the predicted bending of the acoustic branch at the edge of the Brillouin zone. It is worth stressing that this is an effect of the discreteness of the system; in a long Josephson junction, in fact, the acoustic branch has a linear dependence. Experiments have also shown that the inductive term is quite relevant in determining the degree of the bending of the acoustic branch. More spectacularly, it has been demonstrated that, in the linear regime, an optical branch exists when the chain is composed of alternate junctions having two different critical currents [69].

4.3. Vortex motion in the absence of a driving force: ballistic vortex propagation

In underdamped JJAs, because of their mass, vortices should be able to propagate inertially when the driving term is switched off [66]: ballistic propagation. Of course the kinetic energy of the vortex has to be larger than the potential energy, which implies that $v_{min} > \sqrt{E_b}\, l_a \omega_p/\pi$. On the other hand, the vortex velocity also has an upper bound because it must not excite spin waves, $v_{max} \approx 0.1 l_a \omega_p$, as deduced from a continuum model [60]. Up to now there has been just one experiment, on 2D triangular arrays, for

which ballistic motion has been reported [67]. In this experiment, vortices were accelerated in one JJA and then detected in a second, separated from the first by a narrow rectangular JJA channel. The second array was not biased: $I_{dc} = 0$. In the absence of an applied current, and in the approximation of a negligible $\mathrm{d}U/\mathrm{d}x$, the equation of motion of the 'particle' becomes simply $M\dot{v} + \eta v = 0$. From this equation one can deduce an exponential decrease of $v = v_0 \exp(-\eta t/M)$ and a mean free path of the order of $v_0 RC$, much larger than that characteristic of bulk superconductors for which the time constant is very short, 10^{-17} s [23]. For the experiment, it was estimated that $v = 0.016\, l_a \omega_p$, a value somewhat lower than what was expected to be needed to overcome the pinning barrier, $0.043 E_j$; it should have required a peak velocity of $\approx 0.07\, l_a \omega_p$. Nevertheless, vortices may travel much faster than had been estimated, reference [67], at about 2×10^9 lattice spacings per second, so this may not be a problem. The results suggest that ballistic motion is possible just above vortex depinning. Recent results obtained by Fazio *et al* imply a stiffer spin-wave spectrum and a larger window for ballistic motion, up to $v_{max} \approx 0.5\, l_a \omega_p$ [68]. However, to date there are no experimental data that support ballistic propagation of vortices at so high a velocity, in homogeneous 2D arrays. Numerical evidence for ballistic motion in anisotropic ladders has been obtained for when the anisotropy is high enough to yield a small damping coefficient and vortex mass [33]. Since the effect of screening on the ballistic motion has not yet been investigated, we may conclude that this point deserves further investigation.

4.4. Dynamical instabilities and row switching

If we are in the dynamical regime characterized by vortex reflection and we increase β_c further, the vortex dynamics becomes unstable. In numerical simulations we have observed such instabilities in ladders and in more extended 2D arrays. Beyond a certain value of β_c, the vortex reflection region disappears and one passes directly from the vortex annihilation region to the instability region. The critical value of β_c required for this to happen seems to decrease with increase of the vertical size of the array. In 2D JJAs, instabilities are known to induce what it is called a row switch. Since we do not see how this concept can be straightforwardly applied to ladders, in the rest of this section we restrict ourselves to considering instabilities in the 2D JJAs. From the results reported in the literature [71, 26], in 2D arrays row switching is observed only when $f \neq 0$, or if $f = 0$ for $\lambda_\perp \neq \infty$, and what occurs is a switch to the normal state of one or more entire rows of the array; as a consequence a voltage jump as high as $i_{dc} r_e n / N_y$ is observed, where n is the number of switched rows.

Row-switching phenomena have also been imaged and confirmed by LTSEM (see figure 11) [53].

The mechanism of the row switch has not yet been described quantitatively. On a qualitative basis it has been suggested [60] that a row switch occurs because single junctions are in the metastable part of the zero-voltage branch of their I–V characteristics and an external perturbation, like a passing voltage, can initiate a transition to the non-zero voltage branch.

An interesting feature of the row-switch regime is the high degree of coupling between the junctions of the array, leading to the formation of coherent dynamical states in which 'vortices' move in columns. A Fourier analysis of the voltage signal in the row-switch regime shows very sharp peaks and supports the assertion of coherence of this dynamical state [26]. Such a coherent state may be disturbed and even destroyed by a finite value of $\lambda_\perp$. No experimental confirmation of these numerical results has been obtained up to now.

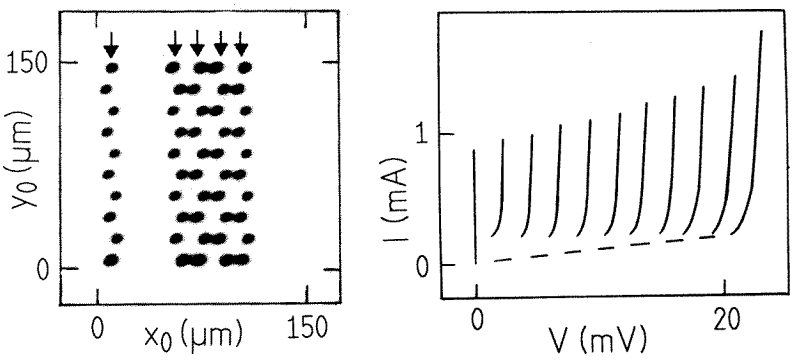

Figure 11. (a) A grey-scale representation of the voltage image $\Delta V(x, y)$ of an underdamped 10×10 array at $\approx$5 K. The dark area indicates a negative electron-beam-induced $\Delta V(x, y)$. Five rows are in the voltage state. (b) The current–voltage characteristic of the array; the LTSEM image of the row-switch state was taken at the fifth step. *Courtesy of Doderer and co-workers [53].*

4.5. Comparison with continuous systems

A long and stacked Josephson junction can be considered as the continuous counterpart of extremely anisotropic JJA arrays. Long Josephson junctions are characterized by several prominent dynamic features in the I–V characteristics [16]:

(a) zero-field steps;
(b) a flux-flow regime; and
(c) Fiske steps.

We have already seen that in discrete arrays one can observe very similar features. Nevertheless, there are some differences. In a discrete system there is always a finite barrier that the vortex has to overcome to move from one plaquette to the next; moreover the vortex excites spin waves in its wake, the dispersion laws are no longer linear and, under certain conditions, optical branches are detectable (see figure 12).

In addition to the above-mentioned characteristics, in stacked long Josephson junctions one also observes:

(d) resonance branches corresponding to different vortex propagation states characterized by different velocities. As an example, with two stacked junctions one observes vortices that propagate along the junctions being locked in phase or out of phase [72].

Some experiments have been performed on extremely anisotropic two-row arrays (also called inductively coupled arrays) and, as for the continuous case, in-phase and out-of-phase vortex propagation modes characterized by two different velocities have been observed [48, 73]. Simulations of bidimensional JJAs have been reported in reference [74]. Many more experiments and simulations relevant to this subject are expected in the near future.

5. Final remarks and future perspectives

This review has we hope given a flavour of the extreme liveliness of the research on vortex dynamics in Josephson junction arrays and, also, of the still numerous open questions, remaining in spite of the huge efforts that have been made during the last five to six years.

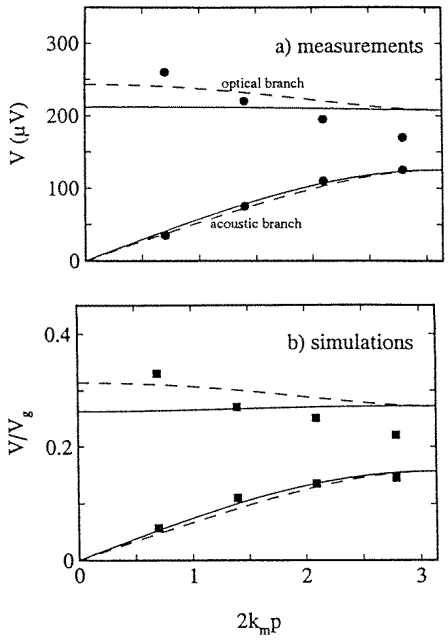

Figure 12. (a) The dispersion relation for the modes of the 1D array measured at 8.5 K in the linear regime. (b) Numerical simulations. Note the bending of the dispersion law at the border of the Brillouin zone and the observation of an optical branch. *Courtesy of van der Zant et al [69].*

Basically, we first described the up-to-date theoretical framework needed to interpret and simulate the experimental results. The Lagrangian was written out for the gauge-invariant phases to show that these are the relevant dynamical variables. From the Lagrangian, then, we derived the equation of motion and showed that it contains both the current-conservation law for the knots and the Biot–Savart equation. This latter is the equation that makes the difference between the XY-formalism and the 'discrete JJ' one, allowing one to account in a complete manner for the mutual inductance of the branch currents and to introduce a finite penetration depth. Starting from this description one can extend the model to include granular superconductors and anisotropic arrays. Also, comparison with other discrete models, such as the discrete sine–Gordon and Frenkel–Kontorova models, becomes easy. Next, we pointed out how, under certain conditions, the phase dynamics can be mapped onto the dynamics of a massive particle that moves in a viscous medium while it is subjected to a periodic potential. This latter is a simple but sometimes very helpful model, providing one with an intuitive feel for the physics.

Once the theoretical bases had been established we reviewed various aspects of the single-vortex dynamics in JJAs, starting with the case of the massless vortices. We first discussed the vortex pinning introduced by the discreteness of the array and showed that the value of the static barrier to the cell-to-cell vortex transfer can be strongly influenced by screening. This latter influences, as well as the dynamical value of the barrier, that of the vortex velocity (the bias current) and, thus, that of the viscosity coefficient. Last, but more importantly, screening influences the vortex size, the key dynamical parameter, which strongly depends also on the vertical extent of the array and on the Josephson coupling asymmetry.

In addition to the size of the vortex, its asymmetric profile may also have a certain relevance. We believe that asymmetry is the indicator of a non-conventional dissipation mechanism that leads to the accumulation of energy in the array and to the development of a vortex cascade and, in turn, to the alternate-vortex motion. Some points still remain unclear—for example, the definition of a relaxation time for a JJA perturbed by a massless vortex—and many more numerical simulations are needed to elucidate the effect of a magnetic field, the detail of vortex formation and annihilation, the vortex–vortex interaction and so on. Also looking very interesting and promising is the investigation of the vortex dynamics in anisotropic JJAs. On the experimental side it is important to point out that only the average effects of the vortex dynamics have been studied. The study of single-vortex dynamics in 'real time' [58] looks to be a challenging issue for the future.

No less appealing, as has been shown, is the study of massive vortex dynamics. The pinning energy depends on the vortex mass and new dynamical regimes have to be considered. The 'launched' vortices do not always annihilate at the edge of the JJA, but, depending on its mass, one can observe vortex reflections and dynamical instabilities. On increasing the vortex energy (i.e. the velocity and/or mass), additional dissipation mechanisms are activated. If these latter are not too intense, ballistic vortex propagation can be observed. Here again, as already discussed in the text, many aspects of the vortex dynamics need further and deeper investigation.

Extremely anisotropic JJAs (inductively coupled JJ arrays) have been shown to be very useful as regards comparing the dynamical properties of discrete arrays with those of their continuous counterparts: long and stacked Josephson junctions. For example, very elegant and efficient investigations of the discrete plasma spectrum have been performed and the shapes of the dispersion curves have been shown to be influenced by the screening effect. The field of research concerned with inductively coupled arrays is quite new and seems promising.

Vortex dynamics in JJAs is thus a field in rapid and intensive evolution, whose limits extend well beyond the 'borders' that we have imposed in the present review to include other aspects of the 'classical' vortex dynamics (such as locking, chaos and turbulence) and, also, many more subjects related to the quantum nature of the vortices [75].

Acknowledgments

The authors wish to thank T Doderer, J V José, R Newrock, N Pedersen, A Ustinov and H J S van der Zant who kindly read the first version of the manuscript and made a number of constructive suggestions.

References

[1] For a recent review on the 'state of the art', see
Giovannella C and Tinkham M (ed) 1995 *Macroscopic Quantum Phenomena and Coherence in Superconducting Networks* (Singapore: World Scientific)
Cerdeira H A and Shenoy S R (ed) 1996 *Physica* B **222** 253

[2] As an introduction to the subject of JJAs, see
Giovannella C and Lambert C (ed) 1998 *Superconductivity in Arrays and Mesoscopic Systems* (New York: AIP) at press
and as general reference books on the physics of Josephson junctions, see
Likharev K K 1986 *Dynamics in Josephson Junctions and Circuits* (New York: Gordon and Breach)
Barone A and Paterno G 1982 *Physics and Applications of the Josephson Effect* (New York: Wiley)
Tinkham M 1996 *Introduction to Superconductivity* (New York: McGraw-Hill)

[3] Strogatz S H and Stewart I 1993 *Sci. Am.* (12) 68
[4] Hebrank F X, Vollmer E, Gutmann P, Müller F and Niemeyer J 1995 *Nonlinear Superconducting Devices and High T_c Materials* ed R D Parmentier and N F Pedersen (Singapore: World Scientific) p 461 and references therein
[5] Likharev K K and Semenov V K 1991 *IEEE Trans. Appl. Supercond.* **1** 3
Nakajima K, Mizusawa H, Sugahara H and Sawada Y 1991 *IEEE Trans. Appl. Supercond.* **1** 29
[6] Mizugaki Y, Nakajima K, Sawada Y and Yamashita T 1993 *Appl. Phys. Lett.* **62** 762
[7] Kadin A M 1990 *J. Appl. Phys.* **68** 5741
[8] Ciria J C, Pacetti P, Paoluzi L and Giovannella C 1996 *Nucl. Instrum. Methods Phys. Res.* A **370** 128 and references therein
[9] Mygind J and Pedersen N F 1995 *Macroscopic Quantum Phenomena and Coherence in Superconducting Networks* ed C Giovannella and M Tinkham (Singapore: World Scientific) p 339 and references therein
[10] Davidson B A, Redwing R D, Nguyen T and Nordman J E 1995 *Nonlinear Superconducting Devices and High T_c Materials* ed R D Parmentier and N F Pedersen (Singapore: World Scientific) p 469 and references therein
[11] Seidel P 1995 *Nonlinear Superconducting Devices and High T_c Materials* ed R D Parmentier and N F Pedersen (Singapore: World Scientific) p 19 and references therein
[12] Müller P 1996 *Physica* B **222** 385
[13] McLaughlin D W and Scott A C 1978 *Phys. Rev.* A **18** 1652
[14] Kivshar Y S and Malomed B A 1989 *Rev. Mod. Phys.* **61** 763
[15] Parmentier R D 1993 *The New Superconducting Electronics* ed H Weinstock and R W Ralston (Dordrecht: Kluwer) p 221
[16] Pedersen N F and Ustinov A V 1995 *Supercond. Sci. Technol.* **8** 389 and references therein
[17] Phillips J R, van der Zant H S J, White J and Orlando T P 1993 *Phys. Rev.* B **47** 5219
[18] Domínguez D and José J V 1994 *Int. J. Mod. Phys.* B **8** 3749 and references therein
[19] Nuvoli A, Giannelli A, Ciria J C and Giovannella C 1994 *Nuovo Cimento* **16** 2045
[20] Nakajima K and Sawada Y 1981 *J. Appl. Phys.* **52** 5732
Majhofer A, Wolf T and Dieterich W 1991 *Phys. Rev.* B **44** 9634
[21] Mon K K and Teitel S 1989 *Phys. Rev. Lett.* **62** 673
Chung J S, Lee K H and Stroud D 1989 *Phys. Rev.* B **40** 6570
Shenoy S R 1985 *J. Phys. C: Solid State Phys.* **18** 5163
[22] van der Zant H S J, Fritschy F C, Orlando T P and Mooij J E 1993 *Phys. Rev.* B **47** 295
[23] Orlando T P, Mooij J E and van der Zant H S J 1991 *Phys. Rev.* B **43** 10 218
[24] Joyez P 1996 Le transistor a une paire de Cooper: un systeme quantique macroscopique *PhD Thesis* Université Paris 6
[25] See for example
Beck H and Ariosa A 1991 *Solid State Commun.* **80** 657 and references therein
The TDGL model seems to be relevant for the interpretation of the noise experiments, according to
José J V 1997 private communication
and, also, to explain the linear behaviour of the I–V characteristic of a capacitive array once the sample has switched to the normal state.
[26] Phillips J R, van der Zant H S J and Orlando T P 1994 *Phys. Rev.* B **50** 9380
[27] Lucheroni C 1997 *Phys. Rev.* B **55** 6559
[28] Ciria J C and Giovannella C 1998 to be published
[29] Giovannella C, Ritort F and Giannelli A 1995 *Europhys. Lett.* **29** 419
Ciria J C and Giovannella C 1996 *J. Phys.: Condens. Matter.* **8** 3057
[30] Davidson A, Dueholm B, Kryger B and Pedersen N F 1985 *Phys. Rev. Lett.* **55** 2059
[31] Peyrard M and Kruskal M D 1984 *Physica* D **14** 88
[32] Bock R D, Phillips J R, van der Zant H S J and Orlando T P 1994 *Phys. Rev.* B **49** 10 009
[33] Ryu S, Yu W and Stroud D 1996 unpublished
[34] Floria L M and Mazo J J 1996 *Adv. Phys.* **45** 505
[35] van der Zant H J S, Rijken H A and Mooij J E 1983 *J. Low Temp. Phys.* **27** 150
[36] Ciria J C and Giovannella C 1997 *J. Phys.: Condens. Matter* **9** 2571
[37] Lobb C J, Abraham D W and Tinkham M 1983 *Phys. Rev.* B **27** 150
[38] Larkin A I, Ovchinnikov Yu N and Schmid A 1988 *Physica* B **152** 266
[39] Eckern U and Schmid A 1989 *Phys. Rev.* B **39** 6441
[40] Rzchowski M, Benz S, Tinkham M and Lobb C J 1990 *Phys. Rev.* B **42** 2041
[41] Hagenaars, Tiesinga P H E, van Himbergen J E and José J V 1994 *Phys. Rev.* B **50** 1143

[42] Trias E, Orlando T P and van der Zant H S J 1996 *Phys. Rev.* B **54** 6568
[43] Kosterlitz J M and Thouless D J 1972 *J. Phys. C: Solid State Phys.* **5** L124
Kosterlitz J M and Thouless D J 1973 *J. Phys. C: Solid State Phys.* **6** 1181
Berezinskii V L 1972 *Zh. Eksp. Teor. Fiz.* **61** 61 (Engl. Transl. 1972 *Sov. Phys.–JETP* **34** 610)
[44] Mazo J J and Ciria J C 1997 *Phys. Rev.* B **68** 16 068
[45] Bobbert P A 1992 *Phys. Rev.* B **45** 7540
[46] Yu W and Stroud D 1994 *Phys. Rev.* B **49** 6174
[47] Ciria J C and Giovannella C 1996 *J. Phys.: Condens. Matter* **8** 7463
[48] Orlando T P, van der Zant H S J, Phillips J R, White J, Trias E and Duwel A E 1995 *Macroscopic Quantum Phenomena and Coherence in Superconducting Networks* ed C Giovannella and M Tinkham (Singapore: World Scientific) p 175
[49] Trias E 1997 private communication
[50] Dominguez D, Gronbech-Jensen N and Bishop A R 1995 *Macroscopic Quantum Phenomena and Coherence in Superconducting Networks* ed C Giovannella and M Tinkham (Singapore: World Scientific) p 278
[51] Ciria J C, Giovannella C, Pacetti P and Paoluzi L 1995 *Macroscopic Quantum Phenomena and Coherence in Superconducting Networks* ed C Giovannella and M Tinkham (Singapore: World Scientific) p 378
[52] Cai Y, Leath P L and Yu Z 1994 *Phys. Rev.* B **49** 4015 and references therein
[53] Lachenmann S G, Doderer T, Hoffmann D and Huebener R P 1994 *Phys. Rev.* B **50** 3158
[54] Hagenaars T J, van Himbergen J E, Tiesinga P H E, José J V and Lachenmann S G 1995 *Macroscopic Quantum Phenomena and Coherence in Superconducting Networks* ed C Giovannella and M Tinkham (Singapore: World Scientific) p 329
[55] Huebener R P 1988 *Advances in Electronics and Electron Physics* ed P W Hawkes (New York: Academic) p 1
Doderer T 1997 *Int. J. Mod. Phys.* B **11** 1979
[56] Lachenmann S G, Doderer T, Huebener R P, Hagenaars T J, van Himbergen J E, Tiesinga P H E and José J V 1998 *Preprint*
[57] Fujimaki A, Nakajima K and Sawada Y 1987 *J. Appl. Phys.* **61** 5471
[58] Giovannella C (coordinator) 1996 Macroscopic quantum particle imaging *TMR Project* N. ERB406PL970543
[59] Ustinov A V, Cirillo M, Larsen B H, Oboznov V A, Carelli P and Rotoli G 1995 *Phys. Rev.* B **51** 3081
[60] Geigenmüller U, Lobb C J and Whan C B 1993 *Phys. Rev.* B **47** 348
[61] Hagenaars T J, van Himbergen J E, José J V and Tiesinga P H E 1996 *Phys. Rev.* B **53** 2719
[62] Bardeen J and Stephens M J 1965 *Phys. Rev.* **140** A1197
[63] van der Zant H S J, Orlando T P, Watanabe S and Strogatz S H 1995 *Phys. Rev. Lett.* **74** 174
[64] Currie J F, Trullinger S E, Bishop A R and Krumhansl J A 1977 *Phys. Rev.* B **15** 5567
[65] Ustinov A V, Cirillo M and Malomed B A 1993 *Phys. Rev.* B **47** 8357
[66] Simanek E 1983 *Solid State Commun.* **48** 1023
[67] van der Zant H S J, Fritschy F C, Orlando T P and Mooij J E 1992 *Europhys. Lett.* **18** 343
[68] Fazio R, van Otterlo A and Schön G 1994 *Europhys. Lett.* **25** 453
[69] van der Zant H S J, Berman D, Orlando T P and Delin K A 1994 *Phys. Rev.* B **49** 12 945
[70] Watanabe S *et al* 1996 *Physica* D **97** 429
[71] van der Zant H S J, Muller C J, Geerlings L J, Harmans P M and Mooij J E 1988 *Phys. Rev.* B **38** 5154
[72] Ustinov A V and Kohlstedt H 1996 *Phys. Rev.* B **54** 6111
[73] Duwel A E, Trias E, Orlando T P, van der Zant H S J, Watanabe S and Strogatz S H 1996 *J. Appl. Phys.* **79** 7864
[74] Petraglia A, Pedersen N F, Christiansen P L and Ustinov A V 1997 *Phys. Rev.* B **55** 8490
[75] Elion W 1995 *PhD Thesis*